AN INVESTIGATION OF THE MECHANICAL STRENGTH OF NANOCRYSTALLINE AU-SI THIN FILMS

By

KYLE DOUGLAS FORD

Bachelor of Science in Mechanical Engineering
Oklahoma State University
Stillwater, OK
2010

Submitted to the Faculty of the
Graduate College of the
Oklahoma State University
in partial fulfillment of
the requirements for
the Degree of
MASTER OF SCIENCE
December, 2012

COPYRIGHT

By

KYLE DOUGLAS FORD

December, 2012

AN INVESTIGATION OF THE MECHANICAL STRENGTH OF NANOCRYSTALLINE AU-SI THIN FILMS

Thesis Approved:

Don A. Lucca

Thesis Adviser

Matthew J. Klopfstein

Hamed Hatami-Marbini

Sheryl Tucker

Dean of the Graduate College

ACKNOWLEDGMENTS

I would like to thank my advisor Dr. Don A. Lucca for giving me the opportunity to learn the process of conducting careful experiments and presenting the results in a manner that is both clear and precise. His guidance and encouragement has made my experience at Oklahoma State particularly valuable for me, and the skills I have developed will serve me well in any environment in which I find myself in the future. I would also like to thank the members of my committee, Dr. M.J. Klopfstein and Dr. H. Hatami-Marbini, for their valuable insights and suggestions. A special thanks is owed to Dr. A. Misra and his colleague, Mr. J.K. Baldwin, at Los Alamos for the synthesis of these films, as well as Mr. J. Modarres for his assistance with the X-ray Diffraction measurements. I would also like to thank my colleagues in the Ultraprecision Surfaces Group, Mr. D. Hildebrand, Mr. S. Qi, Mr. K.M. Schutter, Mr. S.A. Shojaee, Ms. A. Zare and most especially Mr. T.A. Harriman for their assistance and encouragement.

I must thank my wife Bethany, for her encouragement, support and love. I would also like to thank my parents and extended family for all they have done to enable my efforts. I gratefully acknowledge the financial support of the SMART Scholarship.

This material is based upon work supported by the National Science Foundation under Grant Number CMMI-0521989. Any opinions, findings, and conclusions or recommendations are those of the author and do not necessarily reflect the views of the National Science Foundation. This work was performed, in part, at the Center for Integrated Nanotechnologies, a U.S. Department of Energy, Office of Basic Energy Sciences user facility at Los Alamos National Laboratory (Contract DE-AC52-06NA25396). [1]

[1] Acknowledgments reflect the views of the author and are not endorsed by committee members or Oklahoma State University

TABLE OF CONTENTS

1 Introduction **1**

1.1 Motivation for the present study 1

1.2 Objectives 1

1.3 Approach 2

2 Background **3**

2.1 Electrical contact failure mechanisms 3

2.2 Strengthening mechanisms 6

2.2.1 Strengthening by the addition of alloying elements 6

2.2.2 Strengthening from grain boundaries 8

2.2.3 Strengthening from fine particles and other dislocation barriers 10

2.3 Measurement techniques 12

2.3.1 Nanoindentation 12

2.3.2 X-ray diffraction 18

2.3.3 Resistivity measurement 19

3 Experimental **21**

3.1 Specimen preparation and supporting characterization 21

3.2 X-ray diffraction 23

3.3 Atomic force microscopy and nanoindentation 23

3.4 Four point resistivity probe 25

4 Results and discussion **26**

4.1 Composition 26

4.2 Surface topography 27

4.3 Microstructure 28

4.4 Mechanical properties 37

4.5 Strengthening mechanisms 41

4.6 Electrical properties 45

5 Conclusions and future work **49**

5.1 Conclusions 49

5.2 Future Work 50

Bibliography **52**

A Procedure for set up and operation of the atomic force microscope **60**

LIST OF TABLES

2.1 Strength and resistivity of strengthened Au films 13

3.1 Synthesis of Au-Si films 22

4.1 Composition of the Au-Si films determined by PIXE. 27

4.2 Composition of the Au-Si films estimated from deposition parameters. 28

4.3 Roughness of Au-Si films. 30

4.4 Average grain size of Au-Si films determined by XRD. 34

4.5 Average grain diameter determined by TEM. 36

LIST OF FIGURES

2.1 Schematic of a dislocation line passing two incoherent particles. 11

2.2 Comparison of Vickers, Berkovich, and spherical tip geometries. 13

2.3 Typical load function for indentation. 14

2.4 An example load displacement curve and the surface-indenter interface. 15

2.5 Graphic of the indenter surface interface as it is affected by surface roughness. 16

2.6 Effect of loading rate on hardness measurements. 17

2.7 Geometry of interaction between a beam of X-rays and a crystal. 18

2.8 XRD pattern of Au. 19

3.1 Load function and the repeatability of measurements on the pure Au film 24

4.1 Surface topography of films containing 0, 2.5, 6 and 21 at. % Si deposited at 10 Å/s. 29

4.2 Surface topography of films containing 0, 1, 2 and 4 at. % Si deposited at 40 Å/s. . . 29

4.3 Surface topography of films containing 2 at. % Si deposited at 20, 40 and 60 Å/s. . . 30

4.4 Variation of average surface roughness with Si content and deposition rate. 31

4.5 XRD diffraction patterns for films deposited at 10 Å/s. 32

4.6 XRD diffraction patterns for films deposited at 40 Å/s. 32

4.7 XRD diffraction patterns for films containing 2.5 vol. % Si. 33

4.8 Changes in the relative intensity of the Au diffraction peaks. 33

4.9 Plan view TEM images of Au-Si films deposited at 10 Å/s. 35

4.10 The effect of Si content on the hardness and reduced elastic modulus of Au-Si films. 38

4.11 The load function used to minimize creep in the 21 at. % Si film. 39

4.12 The effect of deposition rate on the hardness and modulus of Au-Si films. 40

4.13 The variation in measured hardness of a pure Au film over a range of contact depths. 40

4.14 The correlation between contact depth and average surface roughness. 41

4.15 Hall-Petch plot compiled from experiments from the literature conducted on pure Au films. 42

4.16 Measured and predicted hardness of Au-Si films deposited at 10 Å/s. 44
4.17 Measured and predicted hardness of Au-Si films deposited at 40 Å/s. 44
4.18 Measured and predicted hardness of Au-Si films containing 2 at. % Si. 45
4.19 Resistivity of Au-Si films as a function of Si content and deposition rate. 46
4.20 The trends of electrical conductivity and yield strength. 48

NOMENCLATURE

$A(h_c)$ .... Projected Area

Å .... Angstrom

AFM .... Atomic Force Microscopy

at. % .... Atomic Percentage

b .... Burger's Vector

CINT .... The Center for Integrated Nanotechnologies

E .... Elastic Modulus

EBSD .... Electron Back Scattering Diffraction

E_r .... Reduced Elastic Modulus

FCC .... Face Center Cubic

G .... Shear Modulus

H .... Hardness

h .... Indentation Depth

I .... Current

ISO .... International Organization for Standardization

LANL .... Los Alamos National Laboratory

MEMS .... Micro Electro Mechanical Systems

OFHC .... Oxygen-Free High-Conductivity

PIXE .... Particle-Induced X-Ray Emission

P_{max} .... Maximum Load

Ra .... Mean Roughness

Rq .... Root Mean Square Roughness

Rz .... Maximum Roughness Variation

SEM .... Scanning Electron Microscopy

TEM .... Transmission Electron Microscopy

W_{FWHM} .... Full Width Half Maximum

XRD .... X-Ray Diffraction

V .... Voltage

vol. % .... Volume Percent

wt. % .... Weight Percent

$\Delta\sigma$ .... Change in Yield Stress

λ .... Particle Spacing

ν .... Poisson's Ratio

ρ .... Resistivity

σ .... Yield Stress

σ_i .... Friction Stress

τ_0 .... Shear Stress

Chapter 1

Introduction

1.1 Motivation for the present study

As the trend towards miniaturization of electronics continues, understanding the material properties of the thin films used in the creation of these devices becomes increasingly important. One topic of current research is the development of films for electrical contact surfaces. Recent efforts have proven that these contact surfaces allow the creation of micro-electro-mechanical systems (MEMS) switches with the advantages of low power consumption due to the low mass of the individual switches and minimal size enabling an array of switches to be integrated on one circuit board [1]. These factors make them especially well-suited for space-based communications systems, defense applications, and small electronics, however failure of the contact surfaces has limited their reliability [2]. An understanding of the mechanical strengthening mechanisms operating within these films and their effects on the conductivity of the material is important to the development of reliable switches. If a suitably strong and conductive film could be developed, it would be possible to incorporate these MEMS switches into the next generation of communications electronics, reducing the size, weight, and power consumption as well as increasing the reliability of these systems.

1.2 Objectives

The objective of the present study is to investigate the mechanical properties of Au-Si films as an alternative to pure Au films for use as electrical contact surfaces, as well as the impact of Si addition on the electrical resistivity of these films. Although there have been numerous studies which have successfully created Au films with improved strength, many have observed excessive increases in

electrical resistivity. In order to create a film that is both strong and conductive, the mechanisms responsible for the increase in strength must be fully understood. Additionally, the effect of the composition and microstructure on the resistivity of the film must be taken into consideration. A full understanding of the effects of the processing parameters on the mechanical and electrical properties is necessary for the creation of high-strength, high-conductivity Au-Si films for electrical contact surfaces.

1.3 Approach

In the present work, the mechanical properties of Au-Si films were investigated by nanoindentation. Surface topography was measured using Atomic Force Microscopy (AFM), and the electrical resistivity was measured using a four point resistivity probe. X-ray diffraction (XRD) was used to investigate the crystallographic structure of the films, and Transmission Electron Microscopy (TEM) was performed at the Center for Integrated Nanotechnologies (CINT) at Los Alamos National Laboratory (LANL) which provided information on the microstructure of the films. As an extension of the work of Dvorak [3], an initial set of four Au-Si films deposited at 10 Å/s with Si content up to 21 at. % were investigated to determine the effectiveness of Si addition. Based on results of the initial investigation, attention was focused on films containing less than 5 vol. % Si with deposition rates from 20 to 60 Å/s. The structure of the films was then analyzed to identify and quantify the strengthening mechanisms active within these films. Additionally, the effect of those strengthening mechanisms on the electrical properties of the films was measured.

Chapter 2

Background

2.1 Electrical contact failure mechanisms

Failure of electrical contact surfaces is the focus of many studies in the literature. One area of particular interest is failure of Micro-electro-mechanical systems (MEMS) switches, as these switches are actuated repeatedly under electrical load. An investigation of the causes of the failures observed in MEMS switches should enable the determination of the film parameters that must be improved to prevent premature electrical contact failure. While many switch designs have been introduced capable of millions of cycles, failure of the contact surfaces continues to be an obstacle to the development of reliable MEMS switches [1, 2]. In order to understand the reasons for the failure of the contact surfaces, the basic conditions under which the switch operates should be understood. MEMS switches function by some applied force causing two conductive surfaces to make contact, thereby transmitting the signal. When the force is removed, the switch returns to the open position. The most promising characteristics of MEMS switches, low power consumption and high switching speeds, are only achievable by having low contact forces. Low forces necessitate the use of a highly conductive material which does not form an oxide layer, which is why Au is preferred [4]. However, the ductility and low mechanical strength of Au make it susceptible to stiction or fretting wear [5], which occurs when the two contact surfaces adhere to one another, causing the switch to fail. The most basic failure results in the switch being stuck in the closed position, which occurs when the contact area deforms and bonds together. Spalling is another type of failure in which the force to return the switch to the open position is great enough to remove a section from the surface of one film entirely, leaving it adhered to the surface of the other contact. Failure can also occur when the actual area of contact is much less than the apparent area due to small surface asperities within

the contact region. These asperities can experience localized welding from high current density. When the applied force holding the contact surfaces together is removed, the restoring force pulls the surfaces apart, increasing the height of the asperities until the resistance is too high for reliable contact.

Arrazat et al. [5] performed a study intended to simulate MEMS contact through both static and cyclic contact using a 50 μm radius spherical diamond indenter. In order to understand the level of stress caused by different switching conditions, Arrazat et al. [5] first conducted a series of indentation experiments over a range of loads. The loads were converted to an approximate value of stress using the Hertz contact relation for elastic contact between a sphere and a planar surface. The indentations were subsequently investigated via Electron Back Scatter Diffraction (EBSD), which allowed the Arrazat et al. to observe the grain rotation due to the stress applied by the indenter. These measurements allowed Arrazat et al. [5] to correlate the grain rotation caused by cyclic contact to the equivalent amount of stress induced by a single static load. They observed plastic deformation measurable by atomic force microscopy (AFM) to begin at a stress of 500 MPa, indicated by a flattening effect under the indenter and an increase in the average curvature radius of the asperities. The cyclic load was chosen to represent a stress of 470 MPa applied by a 20 μm radius Au probe, and the switch was operated both with power only applied after contact (cold switched) and with continuously applied power (hot switched) through the contact surfaces. EBSD showed the grain rotation (approximately 30°) which occurred over a half- million cold-switched cycles without applied current was comparable to that of 26,000 hot-switched cycles, and corresponded to a static loading stress of 3 GPa (6 times the applied stress). This indicates that stresses from cyclic contact increase with increasing number of cycles and the application of current through the switch decreases the lifetime significantly. The study presented scanning electron microscope (SEM) images of the surface which showed localized melting and flow away from the contact area, which supports the theory that thermal heating reduces the film strength in the contact region.

Patton and Zabinski [6] conducted an investigation of the factors which cause adhesion of Au contacts by controlling both contact force and electrical current through the contacts. They found that 100 μN was sufficient to create stable contact between Au films deposited on a flat surface and a 1.6 mm diameter sphere, and 10 mA was the upper limit of the switches' current handling ability. Additionally, they noted that adhesion was only an issue with low current, high frequency switching, suggesting that adhesion is a deformation induced condition, where the flattening of the surfaces induces the stiction. As the current was increased, the surfaces retained their roughness, and stiction was not observed. However, when the current was increased to 10 mA localized melting

and the formation of Au nanowires was observed by SEM.

In a study of the relationship between contact force and resistance, Hyman and Mehregany [7] used a sputtered Au spherical anode to make contact with an electroplated Au cathode. In order to prevent contamination, force and contact resistance measurements were taken simultaneously in a nitrogen environment. They observed that deformation was more prevalent in experiments with smaller radius contacts, indicating that the higher current density caused local heating. Hyman and Mehregany [7] also reported that material transfer in the contact region only occurred from cathode to anode, increasing in severity with the applied current. They hypothesized that this process was thermally driven, and the electroplated Au, deposited at a lower temperature than the sputtered Au, would soften at lower temperatures. The researchers noted that the sputtered film had a more refined grain structure as compared with the electroplated film, but did not draw any conclusions about the relative strength of the two films. The Hall-Petch relationship describes an increase in strength with a decrease in grain size [8]. The observed material transfer from the coarse grained electroplated Au to the fine grained sputtered Au film suggests that higher strength films are more resistant to contact failure.

McBride et al. [9] conducted an investigation into the use of carbon nanotubes as a compliant substrate for Au MEMS contact surfaces. A vertically aligned multi-wall carbon nanotube "forest" was first grown on a Si substrate. Then, a layer of Au was sputtered to form the contact surface. In order to test the system, a 500 nm Au film was deposited on a hemispherical probe, and contact was controlled by a piezoelectric actuator. Initial experiments focused on static loading without the application of current through the contacts. A load of 3 mN caused a full collapse of the nanotube structure down to the the Si substrate, resulting in a 60 μm deep crater with the Au contact surface forming cracks around the deformation zone. During hot-switching experiments, an increase in contact resistance was observed which corresponded to delamination of the Au film from the hemispherical probe. At higher currents, both the contact surfaces experienced localized welding resulting in rough patches corresponding to the area of contact.

The previous studies illustrate the need for a stronger Au film for electrical contact applications. Investigations into the effect of surface roughness for these contact materials suggest that the contact surface must not have large surface asperities, which created high contact resistance between the surfaces. However, surfaces which were flattened from repeated contact resulted in flattened surfaces which were prone to sticking together [6], which is undesirable. Arrazat [5] as well as Patton and Zabinski [6] observed local deformation in the contact area due to the repeated cyclic load, which led to an increase in contact area until failure. Increasing the strength of the Au contacts would

reduce the amount of deformation, allowing more reliable operation. Hyman and Mehregany [7] showed that the film with lower strength failed first, indicating that increasing the strength of both contact surfaces should increase the number of switches to failure. Additionally, the results of both Arrazat [5] and Hyman and Mehregany [7] indicate that the thermal effects have an impact on the reliability of Au films, so a thermally stable structure is also preferred.

2.2 Strengthening mechanisms

Advancements in thin film synthesis and characterization techniques in recent years have allowed researchers to investigate materials with specific composition and microstructures. The synthesis of these novel alloys and nanostructured materials has provided insights into the mechanisms responsible for the strengthening of thin films, as well as the effects of those structures on the electrical properties of the films.

2.2.1 Strengthening by the addition of alloying elements

One technique that has been used to strengthen Au films for MEMS contacts is the addition of another metal, including Rh, Ru, Pt, Ag, Pd, Ti, Cr, and Ni [4,10–13]. The creation of a successful alloy incorporates the desirable qualities of each of the individual species while minimizing the more detrimental qualities. The Au alloy films were synthesized to increase the strength of the Au film and retain the electrical properties and resistance to surface oxidation and contamination of the pure Au film.

Lee et al. [10] conducted an investigation into the hardness and resistivity of alloys combining noble metals with Au. The noble metals were chosen for their higher strength and electrical conductivity; however they are susceptible to frictional polymerization after repeated hot switching cycles, which leads to increased contact resistance. Lee et al. [10] hypothesized that a sufficient amount of Au would inhibit the polymerization, as Au is resistant to contamination by oxide layers. Films containing pure Au, Pt, Rh, and Ru, and two alloys of Au with each noble metal were synthesized by sputter deposition. The compositions were chosen to represent a broad range, and no exact chemical measurements were performed. Nanoindentation and four point resistivity probe measurements were performed on each film, allowing the comparison of the mechanical and electrical properties, however each of the alloys except the 10% Pt formed two phase films with higher resistivity than either of the pure constituents. In a previous study, Coutu et al. [4] selected alloy compositions based on phase diagrams, avoiding any combination that would create an intermetallic phase, as well as

any alloy for which a phase diagram was not available. They also avoided creating alloys prone to oxide layers or compositions too close to phase transitions. This narrowed their possibilities to Au alloys with Pt and Ag concentrations less than 15 at. % and Pd concentrations less than 10 at. %. In order to be able to compare the results effectively, baseline films of pure Au, Pt, Pd, and Ag were synthesized as well as three different compositions for each alloy, resulting in thirteen different films for analysis. The films were all deposited using a sputtering technique, and the properties were determined by nanoindentation and four point resistivity probe measurements. The addition of Ag had a negligible effect on the hardness, which is not surprising considering the pure Ag film had a hardness 0.4 GPa less than the Au film. However, the Au-Ag film nearly doubled in resistivity as compared to the pure Au film, which ruled this alloy out as an alternative to pure Au. While the hardness of the Au-Pd alloys increased with increasing Pd content, the Au-6.3 at. % Pt film showed the largest increase in hardness over the pure Au film. In addition, the Au-6.3 at. % Pt film showed the least significant increase in resistivity per at. % of the alloys tested, so this material was selected for further investigation. Coutu et al. [4] proceeded to create MEMS switches with Au contacts and Au-6.3 at. %Pt contacts to compare the performance of these films. Under laboratory conditions, the stronger Au-Pt alloy exhibited a 2.7 times increase in switching lifetime over the pure Au contacts. Coutu suggested that an increase in resistance near the end of the Au-Pt switches testing was evidence of the formation of a contaminate layer, which did not appear in the pure Au switches.

Jahromi [11] found that the hardness of Au films could be increased with the addition of Ti. These Au-Ti films were deposited on Si substrates by electron beam evaporation. Films containing approximately 0, 1, 6, 16, and 20 at. % Ti were found to have a hardness of 1.2, 1.2, 1.1, 2.4, and 3.2 GPa, respectively. However, the resistivity increased linearly from the pure Au value of approximately 3 $\mu\Omega$-cm to 260 $\mu\Omega$-cm, which was attributed to the formation of an intermetallic Au_4Ti phase.

Togasaki et al. [13] investigated an amorphous Au-Ni alloy for use as a contact material in order to develop a material whose strength was independent of the length scale, as the strength of many Au alloys had been determined to be a function of film thickness. The amorphous film was composed of 58 at. % Au with the remaining 42 at. % Ni. The Knoop hardness results show the amorphous film was significantly stronger than either pure Au or conventionally electroplated Au alloys. However, the resistivity of this amorphous film was measured to be 93.3 $\mu\Omega$-cm vs 17.3 $\mu\Omega$-cm for Co hardened Au.

2.2.2 Strengthening from grain boundaries

It is well known that grain boundaries strengthen materials by blocking the movement of dislocations and inhibiting slip [8]. The Hall-Petch equation was originally developed to describe the relationship between yield strength and grain size, and has since been shown to apply to other types of boundaries including twins [8]. It is given as

$$\sigma = \sigma_i + kD^{-1/2} \tag{2.1}$$

where σ_i is the friction stress, k is the locking parameter, and D is the grain diameter in nm. Early investigations into the strength of Au revealed that different deposition methods led to distinct structural differences between the films [14], and variations in strength [15]. The relation between mechanical strength and grain size in pure Au films has been documented by studies using a variety of measurement techniques, with reported Au yield strengths from 115 to 685 MPa [16–25]. Two papers from Lo, Augis, and Pinnel [16, 26] compare the hardness of an electrodeposited Au-0.6 at. % Co film to a sputtered Au film using a Vickers hardness test. Electron beam evaporated Au films of different thicknesses were produced by Cao et al. [17] in order to perform nanoindentation studies on films with grain sizes from 21 to 126 nm. Son et al. [18] also utilized electron beam evaporation to synthesize Au films, but measured strength using a microcantilever beam bending instrument controlled by a nanoindenter to avoid the effects of the substrate. In another study, Huh et al. [19] produced sputtered Au films and utilized an electro-machining technique to fabricate microtensile specimens from the films. Hodge et al. [20] produced an arc-melted Au-Ag alloy which subsequently underwent selective electrolytic dissolution to remove the Ag, leaving behind a nanocrystaline Au foam. This foam was then compressed, leaving behind a nanocrystaline Au specimen which was then tested by nanoindentation. All these studies observed the strength of the Au films to increase with decreasing grain size as described by the Hall-Petch relation. Dieter [8] suggests that caution must be used when the Hall-Petch relation is applied to very small grain sizes, as the dislocation pile-up theory upon which it is based requires the presence of more than 50 dislocations. However, a theoretical investigation by Armstrong et al. [27] determined that the dislocation pile up theory could be applied below the 50 dislocation threshold. When a pile-up begins to form, the increase in strength with each additional dislocation is large. However, as the number of dislocations increases, the effect of each additional dislocation is diminished, and after approximately 50 dislocations, the effect is minimal. This is the reason the Hall-Petch relation initially relied on having at least 50 dislocations in a pile-up, as that allowed the strength due to those dislocations to be considered

to be constant. There remains much debate in the literature regarding the existence of a limit to this relation. The inverse Hall-Petch behavior, in which decreasing grain size below a critical diameter results in lowered strength [27, 28] has been observed in many materials, and there have been numerous theories suggested to explain this behavior [29–31]. Despite these studies, a generally accepted theory capable of explaining the mechanisms responsible for this loss of strength has not been recognised in the literature. Despite the uncertainty as to a lower limit for materials in general, there are experimental studies in the literature on Au alloys at very small grain sizes. A study by Brun et al. [32] of an electrodeposited Au-Cu alloy observed the strength to increase following the Hall-Petch relation down to a grain size of 6 nm, after which the strength decreased. However, Wang et al. [33] reported no breakdown in Hall-Petch behavior of an Au film with minimal Cu additions down to a grain size of 3 nm. Both studies agree that the Hall-Petch relation applies to Au films with grain diameters down to 6 nm.

Another technique that has been used to strengthen thin films is the creation of nanotwinned structures. Twin spacings on the order of nanometers have been observed in Cu [34–37] and Au [38]. As previously mentioned, twin boundaries act in a similar manner as grain boundaries for blocking dislocations, and have been observed to follow the Hall-Petch relationship [8]. Lu et al. [35] observed the strength of nanotwinned Cu to be an order of magnitude higher than coarse grained Cu. Additionally, the resistivity of nanotwinned, nanocrystalline, and coarse grained Cu were compared by Lu et al. [35] as a function of temperature. The resistivity of the nanotwinned Cu and the coarse grained Cu were very near the reported value for oxygen-free high-conductivity (OFHC) Cu, but the resistivity of a nanocrystalline film (grain size of 15 nm) was 1.5 times higher. This illustrates the advantages of nanotwinned structures for high strength, high conductivity applications. Anderoglu et al. [34] reported similar increases in strength, but were also able to show the effect of decreasing twin spacing on the resistivity. They increased deposition rates in order to decrease the average twin spacing. The resistivity of nanotwinned Cu with an average twin spacing of 16 nm was nearly the same as OFHC Cu, while a specimen with an average twin spacing of 7 nm increased the resistivity slightly (0.5 $\mu\Omega$-cm). However, when compared to the increase caused by a nanocrystalline sample (25 $\mu\Omega$-cm), this difference is small. In another study by Anderoglu et al. [39] the thermal stability of nanotwinned Cu was compared to nanocrystalline Cu. The twin spacing/grain size was measured as a function of annealing time, and while both samples showed coarsening, the effect on the nanocrystalline Cu was an order of magnitude larger than that observed on the nanotwins. Grain size increased from 50 nm to 500 nm, while twin thickness increased from 4 nm to 16 nm. Anderoglu et al. [39] showed that nanotwinned structures have the advantages of high resistance to

dislocation movement, low electron scattering, and improved thermal stability.

2.2.3 Strengthening from fine particles and other dislocation barriers

Dieter [8] presents a thorough discussion on strengthening effects of fine particles, a summary of which is presented below.

Fine particles can be incorporated to strengthen materials either by precipitation or dispersion. Precipitation requires an alloy that forms a solid solution at elevated temperature, but has limited solubility at room temperature. After the material is heated to the temperature at which there is a stable solid solution it is quenched, and reheated and held at a lower temperature. Precipitates of the second phase form at the grain boundaries until the material is once again cooled. This is the primary method for strengthening most aluminum alloys. Dispersion strengthening is accomplished by mixing insoluble fine particles into the matrix. Dispersion hardened materials allow more flexibility with material selection, since there is no requirement of changing solubility with temperature. Finely dispersed particles strengthen materials by acting as barriers to dislocation movement. The particle can either act as an impenetrable barrier forcing a dislocation to change directions, or as a coherent particle with increased resistance to dislocation movement over the matrix material. Orowan proposed the strength of dispersion hardened materials containing incoherent particles was governed by the shear stress required to bend a dislocation line between particles, given by

$$\tau_0 = Gb/\lambda \tag{2.2}$$

where G is the shear modulus, b is the Burgers vector, and λ is the particle spacing [8]. Figure 2.1 shows a schematic of a dislocation line as it (a) approaches two particles and (b) begins to bend around them. At (c) the line reaches its minimum radius of curvature, which corresponds to the maximum shear stress required to move past the obstacles.

It can be seen in step (d) that as the dislocation line bends around the particles, it will eventually meet on the other side. The segments that come together will be going in opposite directions, which causes them to annihilate one another in the segments where they meet and reforms the line as shown in (e). This frees the dislocation line to continue to be forced through the material and leaves behind a dislocation loop surrounding each incoherent particle. These loops build up a back stress on other dislocations increasing the shear stress required to push past the particles, which causes strain hardening of the matrix. More refined estimates of dislocation line tensions and corrections for the interaction of particles on either side have led to the development of the Orowan-Ashby

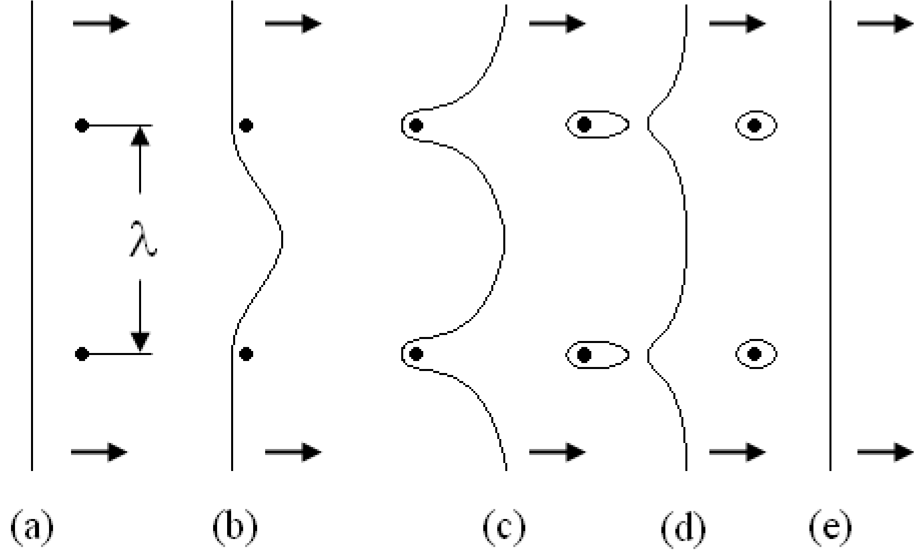

Figure 2.1: Schematic of a dislocation line passing two incoherent particles (adapted from [8]).

equation

$$\Delta\sigma = \frac{0.13Gb}{\lambda} \ln \frac{r}{b} \tag{2.3}$$

which describes the increase in strength based on the shear modulus, Burgers vector, particle spacing λ, and particle radius r.

Dispersion strengthening of Au films has been reported by several authors by the addition of various oxides to the Au film during synthesis. Bannuru et al. [40] used reactive magnetron sputtering to produce Au films with 0, 2.3, and 4 at. % V_2O_5, with measured hardness of 2.5, 3.3, and 4 GPa, respectively. They reported the Au grain size to be approximately 35 nm for all films, thus any strengthening effects were due to the presence of the oxide particles. They observed the resistivity of the 0, 2.3, and 4 at. % V_2O_5 films to be 6, 12.6, and 17.6 $\mu\Omega$-cm, respectively. In addition, the group also synthesized Au-V solid solution films, which had lower hardness and higher resistivity for the same amounts of V when compared to the oxide strengthened films.

Reactive oxide sputtering was also used by Williams and Clarke [41, 42] to create Au-ZrO_2 films with approximately 2.5 vol. % ZrO_2. The films were annealed after synthesis to reduce the resistivity. The hardness of these films measured by nanoindentation was 3.8 GPa, compared to 2.3 GPa for a pure Au sputtered film which had also been annealed. Williams and Clarke [41, 42] attributed the high hardness of the pure Au film to the use of a cube corner tip rather than a Berkovich tip.

However, Chudoba et al. [43] conducted a study comparing nanoindentation results from both tip geometries and concluded the results were comparable as long as the area function and machine compliance were properly calibrated. It is also possible that the hardness of the pure Au film synthesized by Williams and Clarke [41, 42] had an extremely fine grain structure which led to the observed hardness. The resistivity of the pure Au and Au-ZrO_2 films were reported to be 3.4 and 4.5 $\mu\Omega$-cm, respectively.

Fuschillo and Gimpl [44] used chemical methods to coat both ThO_2 and Al_2O_3 particles with Au, and then the powder was pressed and extruded to create Au wires strengthened by oxide dispersion. Tensile tests were then performed on the wires, and the resulting yield stresses were recorded at temperatures ranging from 25 to 500°C. At room temperature pure Au, Au-3.4 vol. % ThO_2, and Au-6.4 vol. % Al_2O_3 had yield strengths of 185, 183, and 228 MPa. While the ThO_2 particles did not increase the strength at room temperature, the wire was more than twice as strong at 500°C, indicating that the ThO_2 particles improve the thermal stability of Au. The resistivity of pure Au, Au-3.4 vol. % ThO_2, and Au-6.4 vol. % Al_2O_3 were reported to be approximately 2.8, 2.9, and 3.4 $\mu\Omega$-cm, respectively.

In a previous investigation, Dvorak [3] investigated the possibility of strengthening Au films by the addition of Si during synthesis. The two elements were not known to form a stable intermetallic phase at room temperature [45–47]. The hardness was shown to increase from the pure Au value of 1.1 GPa to 2.3 GPa for 6 at. % Si. Higher Si concentrations did not increase the strength significantly. Transmission Electron Microscope (TEM) images showed the segregation of amorphous Si partictles to the boundaries of the Au grains, as well as the presence of nanotwins in select Au grains. The resistivity was seen to increase linearly with the Si content.

Table 2.1 shows the composition, hardness and resistivity of the strengthened Au films presented in this section, in order of increasing measured hardness. Pure Au strength values from each of these sources are also presented for comparison. Studies of pure Au films only or studies which did not present both hardness and resistivity data were excluded.

2.3 Measurement techniques

2.3.1 Nanoindentation

Nanoindentation experiments measure indentation force and displacement simultaneously for depths less than 200 nm. ISO 14577 Parts 1 through 4 describe the test method, verification and calibration

Table 2.1: Strength and resistivity of strengthened Au films

Composition	Hardness (GPa)	Resistivity ($\mu\Omega$-cm)	Source
Au	1.1	3.18	[3]
Au	1.4	3.3	[11]
Au	1.77	3.93	[4]
Au	2.5	6	[40]
Au-6.3 at. % Pt	2.19	7.17	[4]
Au-6 at. % Si	2.3	12	[3]
Au-16 at. % Ti	2.7	220	[11]
Au-2.3 at. % V_2O_5	3.3	12.6	[40]
Au-4 at. % V_2O_5	4	17.6	[40]

of testing machines, calibration of reference blocks, and test methods for metallic and non-metallic coatings, respectively [48]. The geometry of the indenter tip must be known in order to be able to interpret the results. Typical indenter tip geometries include four-sided pyramidal Vickers, three sided pyramidal Berkovich and Cube corner, and spherical, shown in Fig. 2.2. The geometry of the Berkovich indenter was developed to give the same projected area as the Vickers indenter for a given depth, while avoiding the chisel tip defect produced when the four sides do not meet at one point.

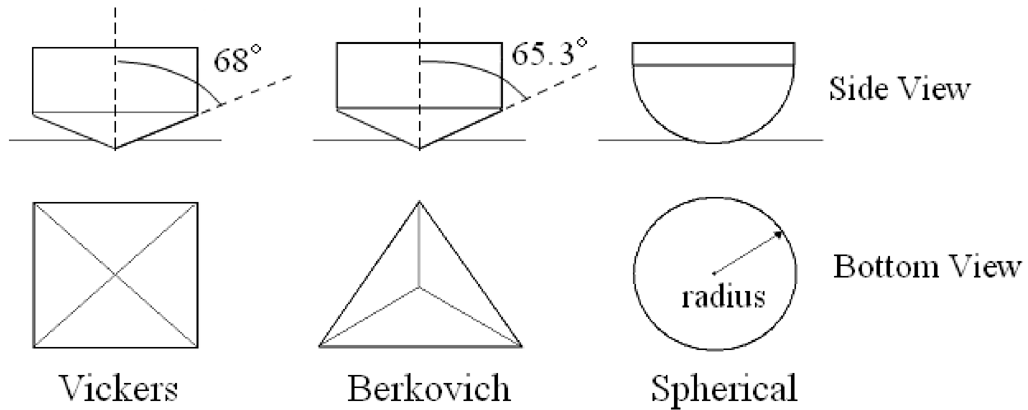

Figure 2.2: Comparison of Vickers, Berkovich, and spherical tip geometries.

Common materials used for indenter tips are diamond, tungsten carbide, and sapphire. During an experiment, either the displacement or, more commonly, the load is controlled. An example

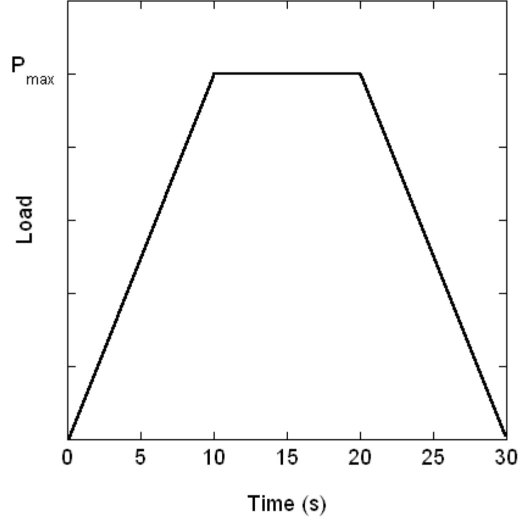

Figure 2.3: Typical load function for indentation.

of the result of a load controlled test using the load function shown in Fig. 2.3 and a corresponding schematic of the interaction between the surface and the indenter, are shown in Fig. 2.4. In Fig. 2.4 (a) the initial loading phase is shown by a), where b) is the hold at P_{max} which reaches a depth of h_{max}. The unloading curve c) crosses the displacement axis at h_f. The intersection of the tangent line to initial slope of the unloading curve d) and the displacement axis is h_r, which is used to determine h_c. The depth of contact h_c is the distance from the tip of the indenter to the point which the surface separates from the tip as labeled in Fig. 2.4 (b). The depth of the permanent impression left by the indenter is represented by h_f.

In order to determine the reduced elastic modulus and the hardness, the contact depth h_c must be known, however it cannot be determined directly from the load displacement plot. Based on the work of Oliver and Pharr [49], the unloading curve is fit to a function of the form $P = K(h - h_f)^m$ where P is the load, and K and m are constants. The derivative of this equation with respect to h is then evaluated at the maximum indention depth which provides the slope of the unloading curve, dP/dh also known as the contact stiffness S, at the instant the unloading segment begins. Contact depth can then be determined by the expression

$$h_c = h_{max} - \epsilon(h_{max} - h_r) \tag{2.4}$$

where ϵ is assumed to be 0.75 for Berkovich and Vickers indenters. The contact depth represents the actual depth at which the indenter was in contact with the surface, and corrects for the surface pulling away from the tip, as shown in Fig. 2.4 (b). A comparison of methods to obtain more

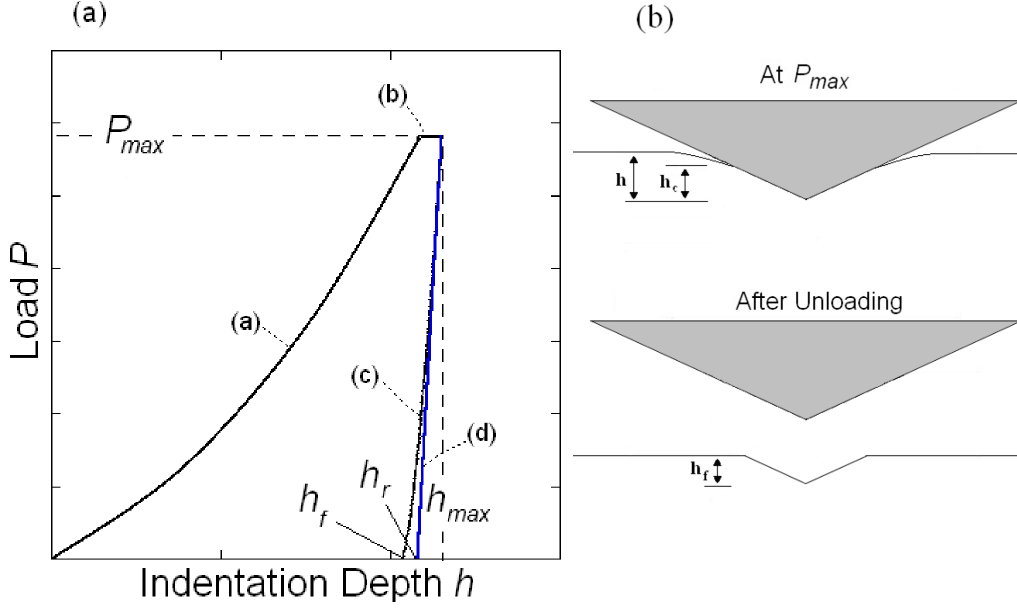

Figure 2.4: (a) An example load displacement curve showing important values obtained during an instrumented indentation test. (b) The surface-indenter interface at P_{max} and after unloading.

accurate values for ϵ is given in Lucca et al. [50], which concludes that the reduced elastic modulus obtained using the estimation for ϵ is 5-10% higher than the actual value. The contact area of a Berkovich indenter can be written as a function of h_c using the procedures outlined in the user manual [51] and ISO 14577-2 [48]. The reduced elastic modulus and indentation hardness can then be found by

$$E_r = S/2 \cdot (\pi/A(h_c))^{1/2} \tag{2.5}$$

$$H = P_{max}/A(h_c) \tag{2.6}$$

where $A(h_c)$ is the projected area of contact at P_{max}, and S is the initial slope of the unloading curve. The reduced elastic modulus contains information about the Poisson's ratio ν and elastic modulus E of both the indenter tip and the material being indented, as shown in Eq. 2.7

$$\frac{1}{E_r} = \frac{1-\nu^2}{E} + \frac{1-\nu_i^2}{E_i} \tag{2.7}$$

where ν and E are the elastic properties of the sample to be determined and ν_i and E_i are the elastic properties of the indenter tip. Diamond is widely used for indenter tips, and has a $\nu_i = 0.07$ and $E_i = 1141$ GPa [48].

Surface Roughness

ISO 14577 specifies that the indentation depth be at least 20 times the Ra in order to minimize the effect of the height variation on the calculated hardness. The effect of surface roughness can be understood by analyzing the three general surface conditions the tip might encounter shown in Fig. 2.5. The ideal situation is flat surface geometry, which is the assumption used for the calculation of contact area and hardness. It can be seen that the contact depth measured from (a) the point the tip touches the surface to (b) the bottom of the indent represents the full depth of the indent, shown in (c). The material under the tip is fully constrained, which allows consistent and accurate measurements to be taken. In the case of contact at the peak of a surface asperity, the depth (c) of the final contact area is approximately that measured by the tip from (a) to (b). The material is less constrained laterally, which results in a deeper residual indent compared to an indent on a flat surface at the same load. A deeper indent results in a higher calculated contact area and a lower calculated hardness (Eq. 2.6). The opposite situation occurs when the tip makes contact between two asperities. The depth (c) of the final contact area is greater than that measured from (a) to (b) due to the surface geometry, which results in a smaller calculated contact area compared with the actual contact area. This is because the actual contact area is a combination of the impression the indenter creates from downward movement and contact with the edges of the asperities. A smaller contact area results in a higher measured hardness as compared with an indent on a flat surface at the same load.

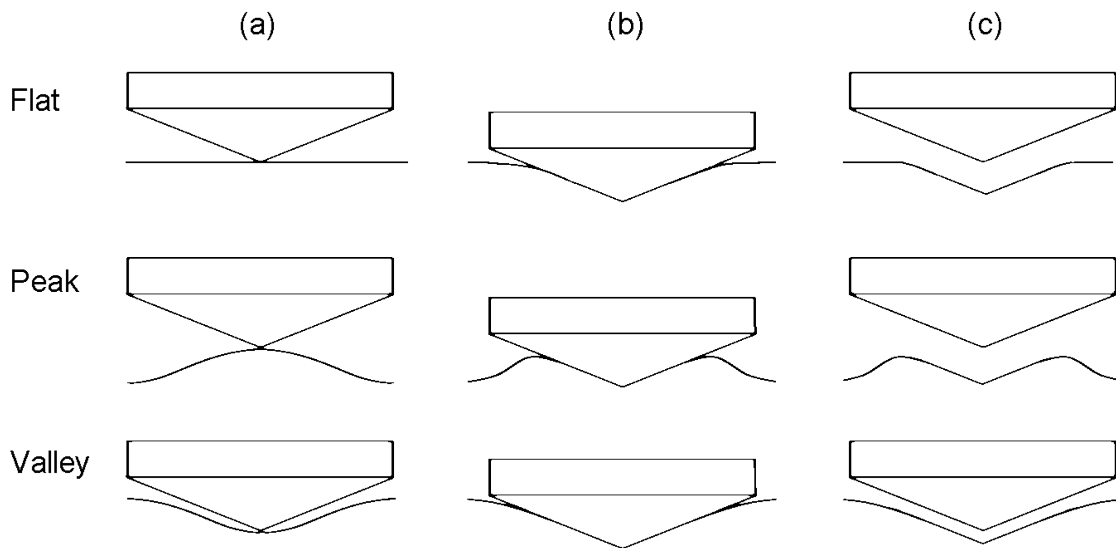

Figure 2.5: Graphic of the indenter surface interface as it is affected by surface roughness.

Strain Rate

The ISO standard 14577 does not specify an acceptable range for loading and unloading rates, instead it requires only the rates be consistent and reported with the results. However, there are several factors that should be taken into account when selecting a load rate. It is important to minimize test time, as the thermal drift correction is measured at the beginning of the experiment and applied to all the data. Chasiotis et al. [52] observed that the yield strength of Au films was consistent between strain rates of 10^{-3} to 10^{-5} s^{-1}, however lower strain rates led to a decrease in the measured strength. A series of indents were performed on fused Si, a standard reference material for nanoindentation, at various load rates as shown in Fig. 2.6, where each point is the average of five individual indents and the error bars represent the maximum and minimum recorded values. It can be observed that low loading rates led to increased variation between measurements. It is unclear if the variation in hardness observed at loading rates below 100 μN/s is significant, as the error bars are larger than the variation between load rates. Additionally, Jonnalagadda et al. [53] reported prolonged creep caused by low strain rates in nanocrystalline Au films, which would lead to errors in the nanoindentation results.

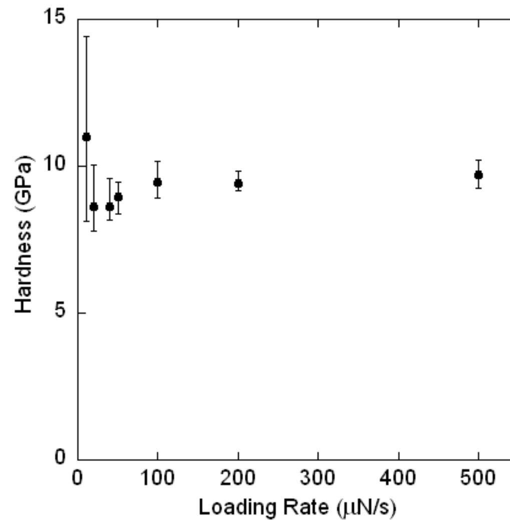

Figure 2.6: Effect of loading rate on hardness measurements.

Size Effects

The indentation size effect has been reported often in the literature and is the subject of many reviews [54, 55]. The basic observation has been an increase in measured hardness with decreasing indentation depth, usually observed by microindentation at depths less than 1 μm. There have

been numerous theories that attempt to explain this behavior. Nix and Gao [56] suggest that the indentation size effect is due to strain gradient plasticity, which describes the increase in hardness using the number of geometrically necessary dislocations contained in the strained volume under the indenter. The hardness increases in order to generate the geometrically necessary dislocations required to satisfy the conditions for deformation. Chakravarthy and Curtin [57] presented another theory which proposes the mechanism responsible for this effect is driven by the stress field under the indenter, which must be great enough to generate dislocations and push them past obstacles. It is important to note that this theory is viewed as complimentary to that of Nix and Gao [56], as a combination of the two could describe the size effect more thoroughly. Both theories rely on the assumption that the dislocations need to be generated in a volume of material that is without the presence of grain boundaries or other dislocation sources. Elmustafa et al. [58] conducted an experiment on coarse grained Al and nanocrystalline Al-Zr, from which he observed the size effect only in the coarse grained sample. Lilleodden and Nix [59] observed a similar trend in Au films, in which coarse grained films showed a Hertzian contact regime followed by a pop-in event, indicative of the onset of plasticity due to a burst of dislocation formation. This was not observed in the fine grained films, which was attributed to the grain boundaries acting as a source for dislocations.

2.3.2 X-ray diffraction

X-ray diffraction (XRD) measures the diffraction angle and intensity of a beam of X-rays with a known wavelength in order to gain information about the composition, orientation and texture of a material. In addition, information can be provided about the grain size of a material. A schematic showing the geometric relationship between a beam of X-rays and a crystal is shown in Fig. 2.7.

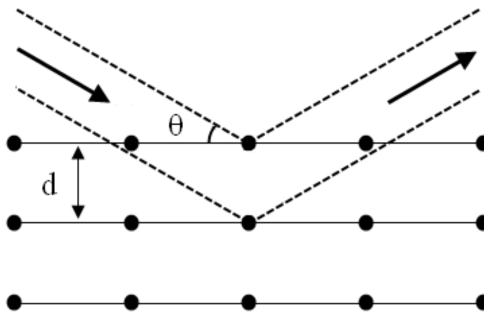

Figure 2.7: Geometry of interaction between a beam of X-rays and a crystal.

Bragg's Law describes the relation between wavelength λ, d-spacing, and diffracting angle θ [60], as shown in Eq. 2.8.

$$\lambda = 2d\sin(\theta) \tag{2.8}$$

X-rays are generated from a source and directed at a sample of the material to be investigated. These X-rays have a characteristic wavelength determined by the source. If the d spacing does not satisfy Bragg's Law, the X-rays diffracted from different planes will be out of phase, and the diffracted intensity will be low. However when the extra distance traveled by the X-rays diffracted from lower planes is a multiple of the wavelength, the X-rays are in phase and constructive interference occurs, which leads to a higher diffracted intensity at that angle. The detector is rotated around the sample in order to record the intensity at a range of diffraction angles, which is then used to generate a plot similar to Fig. 2.8. The location of the peaks correspond to specific crystallographic orientations, and can be used to determine the type of crystalline material illuminated by the beam.

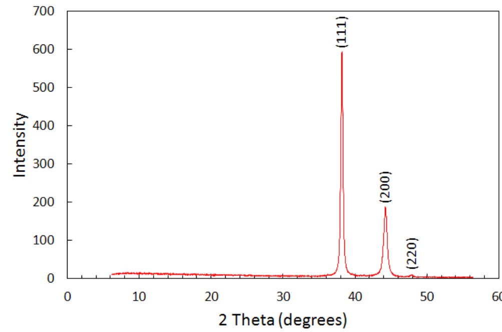

Figure 2.8: XRD pattern of Au.

The Scherrer equation can be used to estimate the grain size of the material [60]

$$d_{average} = \frac{K\lambda 180}{W_{\mathrm{FWHM}}\cos(\theta)\pi} \tag{2.9}$$

where $d_{average}$ is the average depth of the grains perpendicular to the diffracting plane, K is a constant assumed to be 0.94, λ is the incident wavelength, W_{FWHM} is the width of the diffraction peak at half the maximum intensity in degrees, and θ is the diffraction angle. This estimate is the average grain depth in the illuminated area, which includes both grains on the surface of the material as well as those grains within the material.

2.3.3 Resistivity measurement

Resistivity is a measurement of a material's resistance to the flow of electrical current, and is used to compare the effectiveness of that material to conduct electricity. One method used to measure resistivity is the four point resistivity probe, in which a single line of four equally spaced sharp

probes are brought in contact with the surface. Current is then applied across the two outer pins and the voltage drop across the inner pins is measured. The resistivity is calculated by

$$\rho = \frac{\pi}{ln(2)} \frac{V}{I} \cdot t \cdot G_C \tag{2.10}$$

where t is the film thickness and G_C is the geometric correction factor. The geometric correction factor is based on probe geometry and the ratio of probe spacing to sample diameter, as well as the ratio of probe spacing to sample thickness. Geometric correction factors for various geometries and thicknesses have been tabulated by Smits [61].

Resistivity is known to follow Matthiessen's rule [34],

$$\rho_{total} = \rho_t + \rho_i + \rho_d \tag{2.11}$$

where the total resistivity ρ_{total} is the sum of the contributions from thermal vibrations ρ_t, impurities ρ_i, and lattice defects ρ_d. Lattice defects in thin films occur at grain boundaries, twin boundaries, insoluble particles, and the surface of the film.

Chapter 3

Experimental

As previously stated, the objective of the present study is to investigate the mechanisms responsible for the strength of Au-Si films. Specific attention is placed on the impact of microstructure on the strength and resistivity of the films. All films were produced by electron beam evaporation. The initial set of Au-Si films deposited at 10 Å/s were previously investigated by Dvorak [3], and subsequently characterized by transmission electron microscopy (TEM) and particle-induced X-ray emission (PIXE), which provided detailed information on the microstructure and composition. These measurements have been re-evaluated in this investigation, and extended to include results from a second set of films synthesized at higher deposition rates. Atomic force microscopy (AFM) and X-ray diffraction (XRD) measurements were performed on every film to provide information on the topography and structure of the films. Following characterization, nanoindentation and four point resistivity probe experiments were performed on each film to obtain the mechanical and electrical properties of the films.

3.1 Specimen preparation and supporting characterization

Two sets of Au-Si films were prepared at the Center for Integrated Nanotechnologies (CINT) at Los Alamos National Laboratory (LANL). The films were deposited by co-evaporation of Au and Si onto (100) Si substrates using a commercial electron beam evaporator operating at room temperature with a base pressure between $2-4\times10^{-7}$ Torr. Prior to co-evaporation, a 10 nm thick Ti adhesion layer was deposited onto the substrates. Then Au and Si were simultaneously deposited to produce composite films with thicknesses of approximately 1000 nm. For simplicity films will be referred to using the nomenclature Au(deposition rate)Si(Si content), e.g. the film synthesized by depositing

Au at 10 Å/s and 2.5 at. % Si is denoted as Au10Si2.5. The Si content of films deposited at 10 Å/s was determined by PIXE, and the Si content of all other films was estimated from the deposition parameters as described in Section 4.1. As an extension of the work of Dvorak [3], Au films containing 0, 2.5, 6, and 21 at. % Si deposited at 10 Å/s were investigated. In order to further investigate the effect of changing Si content, films containing up to 4 at. % Si deposited at 40 Å/s (Au40Si0, Au40Si1, Au40Si2 and Au40Si4) were synthesized with nominal Si contents of 0, 1, 2 and 4 at. %, respectively, holding the deposition rate of Au at 40 Å/s. In order to investigate the effect of changing deposition rate, two additional films containing 2 at. % Si (Au20Si2 and Au60Si2) were synthesized at deposition rates of 20 and 60 Å/s, respectively. Table 3.1 presents information on the deposition and Si content of each of the films.

Table 3.1: Synthesis of Au-Si films

Film	Deposition Rate (Å/s) Au/Si	Nominal Si Content vol. %
Au10Si0	10/0	0
Au10Si2.5	9.8/0.2	2
Au10Si6	9.5/0.5	5
Au10Si21	7.5/2.5	25
Au20Si2	20/0.5	2.5
Au40Si0	40/0	0
Au40Si1	40/0.5	1.25
Au40Si2	40/1	2.5
Au40Si4	40/2	5
Au60Si2	60/1.5	2.5

After synthesis of the first set of 1 μm thick Au-Si films deposited at 10 Å/s PIXE was performed at CINT to determine the actual composition present in the films. In addition, 30-50 nm thick films were deposited on NaCl substrates using the same deposition parameters as the Au-Si films deposited at 10 Å/s. The films were then floated off the substrates onto grids for TEM characterization at CINT at LANL to determine the microstructure. Selected area diffraction (SAD) was also performed on these thin films to investigate the nature of the Si particles.

3.2 X-ray diffraction

Information on the crystallographic orientation of the films was obtained from XRD results. XRD was performed using a Bruker D8 Discover XRD2 micro-diffractometer with a Hi-star 2D area detector using a $Cu - K\alpha$ tube source with tube parameters of 40 mA and 40 kV. A spot size of 500 μm allowed a large number of grains to be investigated, and an exposure time of 60 seconds per frame allowed intensities to be recorded for each Au diffraction peak. Sample height alignment was performed with the video-laser system, and the detector to sample distance was 29.97 cm. Diffraction data was collected over the range of 2θ from 15° to 66°, and compared with the standard polycrystalline Au pattern [62].

3.3 Atomic force microscopy and nanoindentation

A diDimension® 3100 AFM was used to perform all AFM measurements. Reported surface roughness values are the average of five 1 μm by 1 μm scans. Each scan was analyzed using the system software to remove the effect of film curvature. Then Ra, Rq, and Rz values are calculated for each image.

Nanoindentation experiments were performed using a Hysitron TI 900 Triboindenter with a Berkovich diamond tip. The Berkovich tip is a three sided pyramidal indenter with a 65.3° face angle, having the same projected area to depth ratio as a Vickers indenter [48]. The instrument compliance and indenter area function were obtained in accordance with ISO-14577 [48] by performing indentations in fused silica and tungsten. The instrument and specimen were allowed to thermally equilibrate for 10-12 hours inside the instrument's thermal enclosure prior to beginning experiments. The drift rate was checked before indenting to confirm that it was less than 0.1 nm/sec averaged over a 5 sec interval. A three segment load function with a 10 second hold at peak load, as shown in Fig. 3.1 (a), was used for each experiment. The loading and unloading rates were held constant at 200 μN/s to avoid the effects of changing strain rates, and the peak load was chosen to correspond to a depth of 10% of the film thickness in order to avoid the effects of the substrate. An example of the repeatability of the load displacement results over 5 experiments is shown in Fig. 3.1 (b). Figure 3.1 (c) shows the creep rate as a function of hold time at the maximum load, measured for the film deposited at 10 Å/s with 21 at. % Si. The hold at maximum load was chosen to minimize the effects of creep, while also maintaining a testing time as short as possible. The creep rate was seen to be approximately 0.9 nm/s initially, however it decreased to 0.26 nm/s at 10

seconds. The effect of hold time on reducing creep rate was observed to be less significant at hold times longer than 10 seconds. As the thermal drift is measured before the test begins, minimizing the test time is important to ensure that the thermal drift correction is accurate. A 10 second hold period at the maximum load allowed the creep rate to decrease significantly while keeping the experiment time short in order to have an accurate thermal drift correction. The ISO standard also suggests that the contact depth be at least 20 times the average surface roughness, which is not always possible with thin film systems. In this work, the effect of surface roughness on the accuracy of the nanoindentation measurements was investigated for all films. Each experiment produced a load displacement curve, which was analyzed using Hysitron's Triboscan software. The software uses the procedure developed by Oliver and Pharr [49] and the calibrated area function to calculate the reduced elastic modulus and hardness of the film. A detailed explanation of the use of this program can be found in the user manual [51].

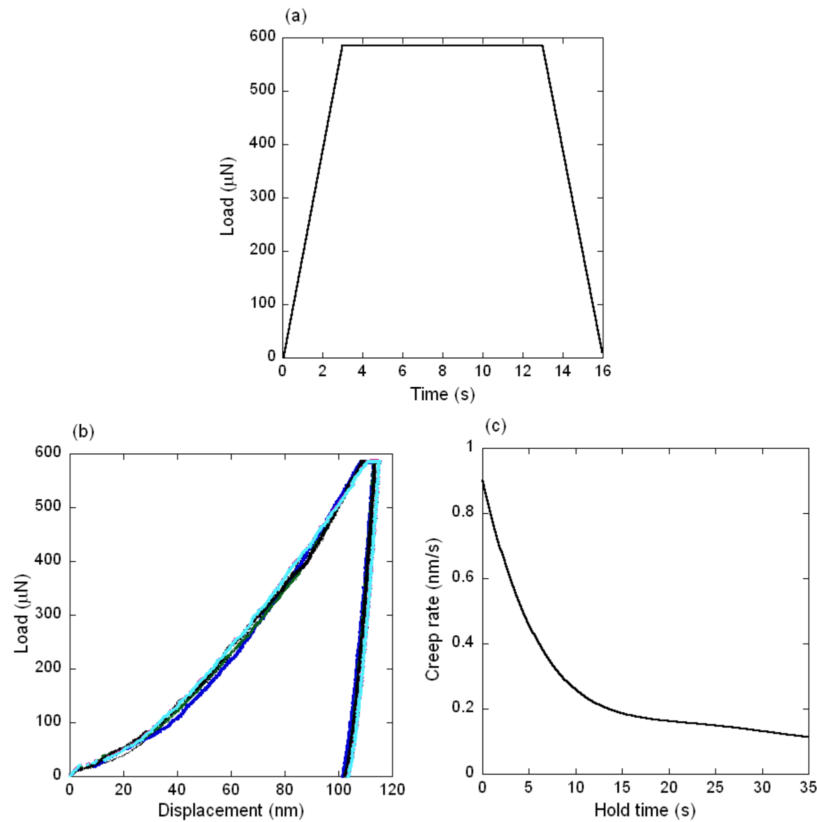

Figure 3.1: (a) Load function used for all nanoindentation experiments, and (b) an example of the repeatability of 5 load controlled measurements on the pure Au film. (c) The creep rate as a function of hold time at maximum load.

3.4 Four point resistivity probe

Resistivity measurements were performed using a Veeco FPP-5000 four point resistivity probe. This instrument provides a constant probe force independent of the operator force and wafer thickness by lowering the wafer towards stationary probes [63]. It is accurate to within 0.5% of resistance values from 5 mΩ to 5 kΩ. In order to measure the ratio of voltage to current needed to calculate the resistivity from Eq. 2.10 the sample was placed on the stage and the lid was pressed closed, bringing the sample in contact with the probe heads. Each recorded value is the average of four measurements, with the sample being rotated 90° after each measurement. Due to the size of the samples, it was necessary to use a geometric correction factor as shown in Eq. 2.10 based on probe spacing and sample dimensions [61]. For these experiments the films were deposited on a 3 inch Si wafer that was subsequently cleaved to produce a number of samples, thus an additional geometric correction factor of 0.95-0.9875 was applied to correct for the finite dimensions of the film.

Chapter 4

Results and discussion

This chapter presents the results of the investigation into the effects of Si content and deposition rate on the mechanical and electrical properties of Au-Si films. After synthesis, Particle-induced X-ray emission (PIXE) and transmission electron microscopy (TEM) with selected area electron diffraction (SAD) were performed at the Center for Integrated Nanotechnologies (CINT) at Los Alamos National Laboratory (LANL) on the Au-Si films deposited at 10 Å/s to determine the composition and microstructure of the films. Information about surface roughness and topography was provided from atomic force microscopy (AFM) scans on all the films, and the results of the X-ray diffraction (XRD) investigations revealed details about the structure of each of the films. Nanoindentation data provided information on the hardness and reduced elastic modulus of each film. The grain size as well as Si particle size and spacing of each film was used to estimate its strength, and those estimates were compared directly to the experimental data obtained from nanoindentation. Additionally, the results of the four point resistivity probe measurements provided information on the electrical resistivity of each of the films, which was then compared to other high-strength Au films.

4.1 Composition

Original measurements of surface topography, XRD, hardness and modulus, as well as resistivity of Au-Si films deposited at 10 Å/s were performed by Dvorak [3]. For these films, composition was determined at CINT at LANL by PIXE, and thin film specimens were also fabricated to permit plan view TEM imaging. In this work each of the films have been re-evaluated, and these measurements have been extended to include a second set of Au-Si films deposited at higher deposition rates.

PIXE was performed at CINT at LANL on the Au-Si films deposited at 10 Å/s after synthesis, which measured the actual Si concentration in atomic percent (at. %) present in the films deposited at 10 Å/s, as shown in Table 4.1.

Table 4.1: Composition of the Au-Si films determined by PIXE.

Film	Deposition Rate (Å/s) Au/Si	Nominal Si Content vol. %	Si Content determined by PIXE at. %
Au10Si0	10/0	0	0
Au10Si2.5	9.8/0.2	2	2.5
Au10Si6	9.5/0.5	5	6
Au10Si21	7.5/2.5	25	21

Measurements of the actual composition of the second set of Au-Si films synthesized at higher deposition rates have not been performed, however the atomic percent can be estimated by converting the volume percent (vol. %) to weight percent (wt. %) using Eq. 4.1 [64],

$$\text{wt. \% Si} = \frac{\rho_{\text{Si}}}{\rho_{\text{film}}}\,(\text{vol. \% Si}) \tag{4.1}$$

where ρ_{Si} is the density of Si and ρ_{film} can be found using Eq. 4.2.

$$\rho_{\text{film}} = (\text{vol. \% Si})\,\rho_{\text{Si}} + (\text{vol. \% Au})\,\rho_{\text{Au}} \tag{4.2}$$

The density of Si (ρ_{Si}) is 2.28 g/cm^3 [65, 66] and the density of Au (ρ_{Au}) is 19.3 g/cm^3 [65]. Atomic percent can then be found using Eq. 4.3,

$$\text{at. \% Si} = \frac{(\text{wt. \% Si})/\text{M}_{\text{Si}}}{(\text{wt. \% Si})/\rho_{\text{Si}} + (\text{wt. \% Au})/\text{M}_{\text{Au}}} \tag{4.3}$$

where M_{Si} and M_{Au} are the atomic masses of Si (28.09 g/mol) and Au (196.97 g/mol), respectively. The estimated composition of each of the second set of Au-Si films is shown in Table 4.2

4.2 Surface topography

Atomic force microscopy (AFM) was performed on each film to investigate the surface topography. Images of the surfaces of films deposited at 10 Å/s and 40 Å/s with different Si concentrations are shown in Figs. 4.1 and 4.2, respectively. Nodular surface topography is present on each of the surfaces, which has been observed previously in the literature [67]. The height variation of these films was observed to increase as Si content increases. Figure 4.3 shows the evolution of surface morphology

Table 4.2: Composition of the Au-Si films estimated from deposition parameters.

Film	Deposition Rate (Å/s) Au/Si	Nominal Si Content vol. %	Si Content (estimated) at. %
Au20Si2	20/0.5	2.5	2
Au40Si0	40/0	0	0
Au40Si1	40/0.5	1.25	1
Au40Si2	40/1	2.5	2
Au40Si4	40/2	5	4
Au60Si2	60/1.5	2.5	2

with increasing deposition rate, where the Si concentration was held constant at 2 at. %. The height variation was observed to remain constant for films deposited at 20 and 40 Å/s, then decrease for the film deposited at 60 Å/s. The AFM scans were anylized to provide information about the surface roughness of each of the films. Surface roughness was calculated using three different algorithms, which relate the height of the asperities measured over the scan area. Ra is the arithmatic average of the asperity heights, whereas Rq is the root mean square of the asperity heights. Rq is the maximum height of the asperities on the surface. Table 4.3 shows the surface roughness of each film, where each reported value is the average of five 1 μm by 1 μm scans. Figure 4.4 shows the changes in average surface roughness (Ra) as a function of (a) Si content as well as (b) deposition rate, where the error bars represent the maximum and minimum measured roughness values. The average surface roughness was observed in Fig. 4.4 (a) to increase as a function of Si content up to approximately 6 at. % Si for the films deposited at 10 Å/s, after which there is little change. The films deposited at 40 Å/s also increase with increasing Si content, however the Ra of the 4 at. % Si film is 17.8 nm as compared with 8.0 nm for the film deposited at 10 Å/s containing 6 at. % Si. In the three films containing 2 at. % Si, the average surface roughness was observed to decrease with increasing deposition rate as shown in Fig. 4.4 (b).

4.3 Microstructure

X-ray diffraction (XRD) was performed on each film to gain insight into the crystallographic structure of each of the films. Figures 4.5 and 4.6 and show the diffraction patterns for films deposited at 10 Å/s and 40 Å/s respectively, with increasing Si content. The strong peak located at the

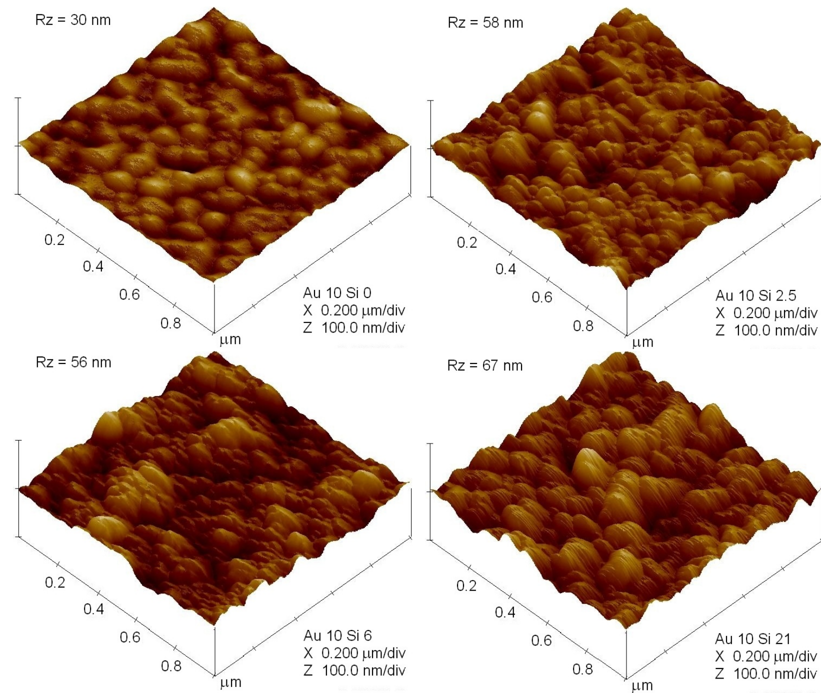

Figure 4.1: Surface topography of films containing 0, 2.5, 6 and 21 at. % Si deposited at 10 Å/s.

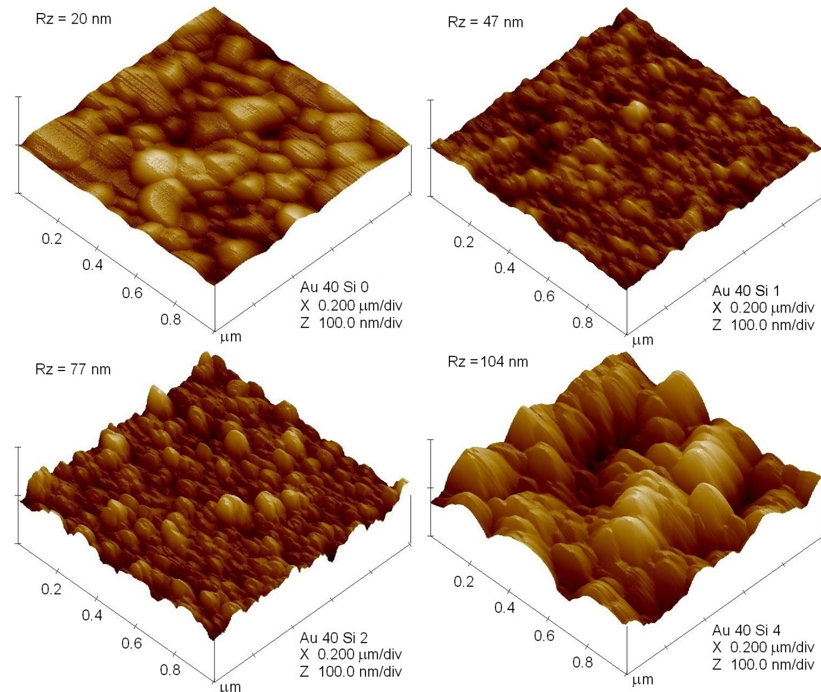

Figure 4.2: Surface topography of films containing 0, 1, 2 and 4 at. % Si deposited at 40 Å/s.

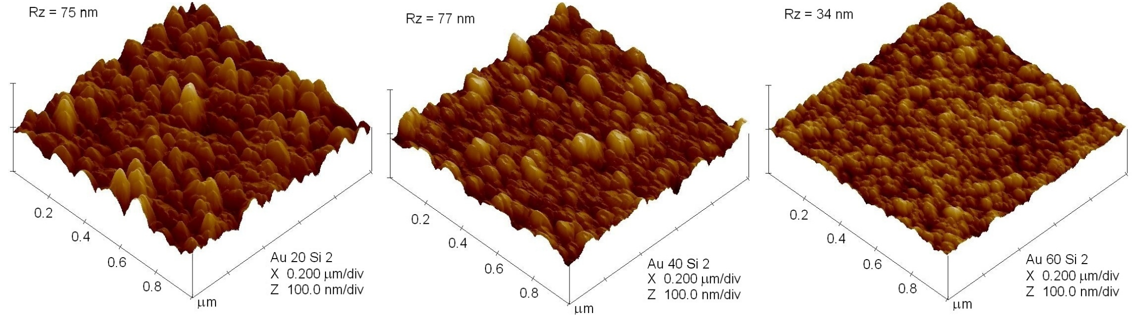

Figure 4.3: Surface topography of films containing 2 at. % Si deposited at 20, 40 and 60 Å/s.

Table 4.3: Roughness of Au-Si films.

Film	Rq (nm)	Ra (nm)	Rz (nm)
Au10Si0	3.9	3.0	30
Au10Si2.5	7.4	5.7	58
Au10Si6	8.0	6.4	56
Au10Si21	9.0	7.1	67
Au20Si2	10.2	8.1	75
Au40Si0	3.0	2.4	20
Au40Si1	5.4	4.2	43
Au40Si2	9.4	7.3	77
Au40Si4	17.8	14.4	104
Au60Si2	4.6	3.7	34

angle $2\theta = 38.2°$ corresponds to the (111) diffraction peak of Au, and was observed to have the highest intensity in each of the Au-Si films. The (200) and (220) Au diffraction peaks (located at $2\theta = 44.6°$ and $64.5°$) were also observed in all films, however the relative intensities of these three peaks were observed to change with film composition and deposition rate. The difference is shown in Fig. 4.6 by the diffraction patterns for the pure Au film (Au40Si0) and the 4 at. % Si film (Au40Si4). The diffraction peaks corresponding to the (200) and (220) planes of the pure Au film deposited at 40 Å/s are over 1000 times less intense than the (111) peak, whereas the same peaks are close to 1/3 the intensity of the (111) peak for the 4 at. % Si film. The same trend is seen for the films deposited at 10 Å/s in Fig. 4.5, however there is little change in the intensities from the 6 at. % to the 21 at. % Si film. A similar trend was observed in the surface roughness,

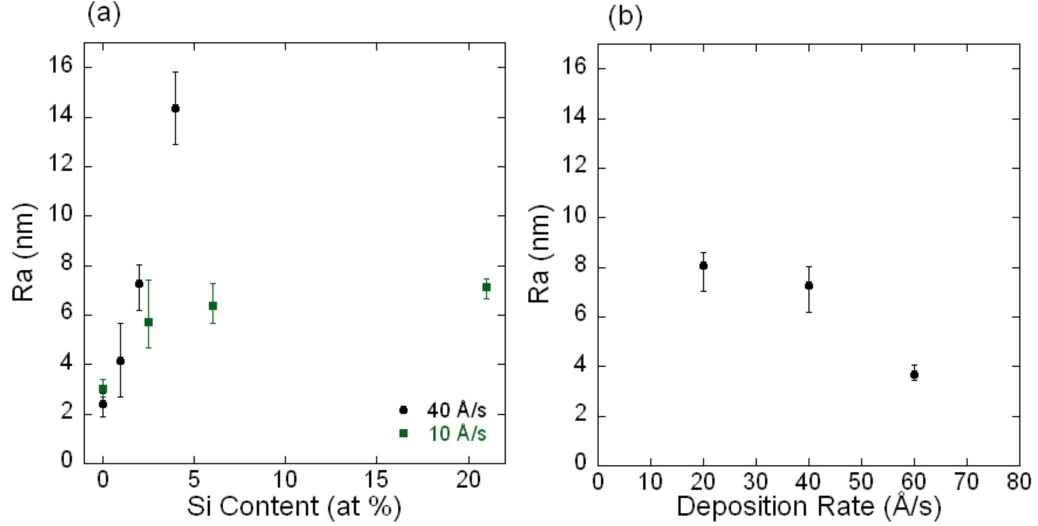

Figure 4.4: Variation of average surface roughness (Ra) with (a) Si content and (b) deposition rate.

where roughness increased up to 6 at. % Si, and then showed little change with further increase in Si content. Figure 4.7 shows the observed increase in the intensity of the (200) and (220) peaks with increasing deposition rate when the Si concentration is held constant. No evidence of crystalline Si was observed in the diffraction patterns of any of the films.

The diffraction pattern of both the pure Au films showed the relative intensity of the (111) Au diffraction peak with respect to the (200) Au diffraction peak to be higher than that of the randomly oriented Au Powder Diffraction File [62] which indicated a preferred (111) orientation. The same preferred orientation has been observed in both Cu and Au films synthesized by physical vapor deposition [37,67–69]. The ratio of the (111) Au diffraction peak relative to the (200) Au diffraction peak was observed to decrease with increasing Si content as shown in Fig. 4.8 (a). A decrease in the relative intensity of the (111) Au diffraction peak indicates that the fraction of Au grains aligned in the (200) direction increases with increasing Si content, approaching the distribution of randomly oriented polycrystalline Au, shown in Figs. 4.8 (a) and (b) by the dashed line. This shift away from preferred (111) orientation toward random orientation was also observed with increasing deposition rate as shown in Fig. 4.8 (b).

The (111) Au diffraction peak width was observed to broaden with increasing Si content. Increasing peak width can indicate a reduction in grain size. The grain size can be estimated using Eq. 2.9, where $d_{average}$ is the average grain depth, K is a constant assumed to be 0.94, λ is the incident wavelength (1.54151 Å for $Cu - K\alpha$), W_{FWHM} is the width of the diffraction peak at half the

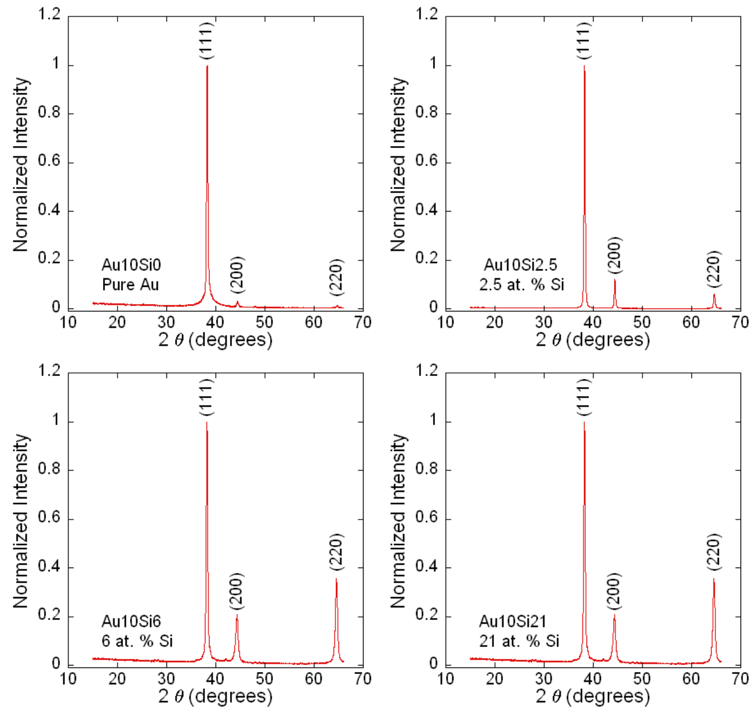

Figure 4.5: XRD diffraction patterns for films deposited at 10 Å/s containing increasing amounts of Si.

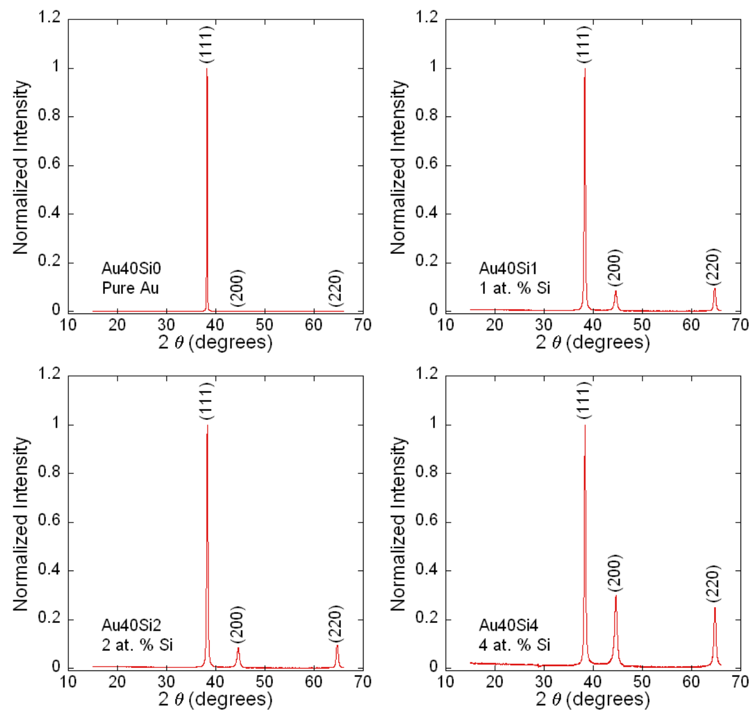

Figure 4.6: XRD diffraction patterns for films deposited at 40 Å/s containing increasing amounts of Si.

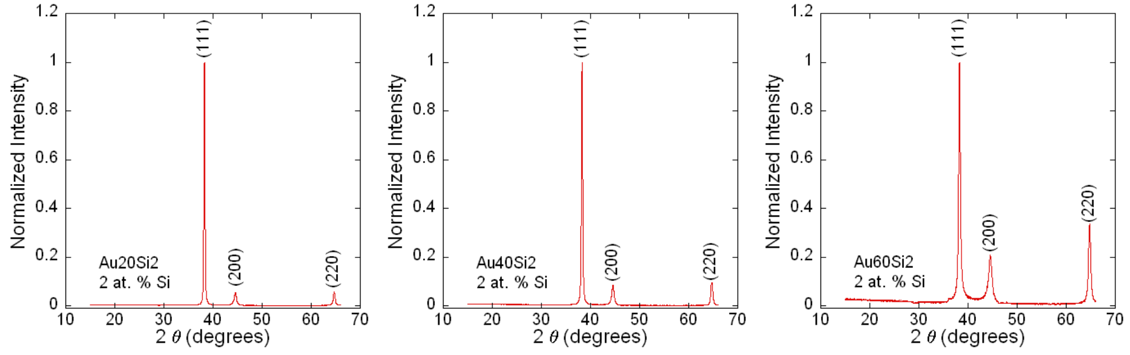

Figure 4.7: XRD diffraction patterns for films containing 2.5 vol. % Si deposited at 20, 40 and 60 Å/s.

maximum intensity in degrees 2θ, and θ is the diffraction angle (19.1° for the (111) plane of Au [62]). If the grains are approximated as equiaxed, the average grain diameter can be approximated as the average grain depth. Table 4.4 lists the W_{FWHM} and average grain diameter for each of the films. These values for $d_{average}$ are similar to those reported in the literature for Au films [16–25]. A decrease in average grain size was observed with increasing Si content for films deposited at both 10 Å/s and 40 Å/s. This decrease in grain size is consistent with the observed decrease in hardness

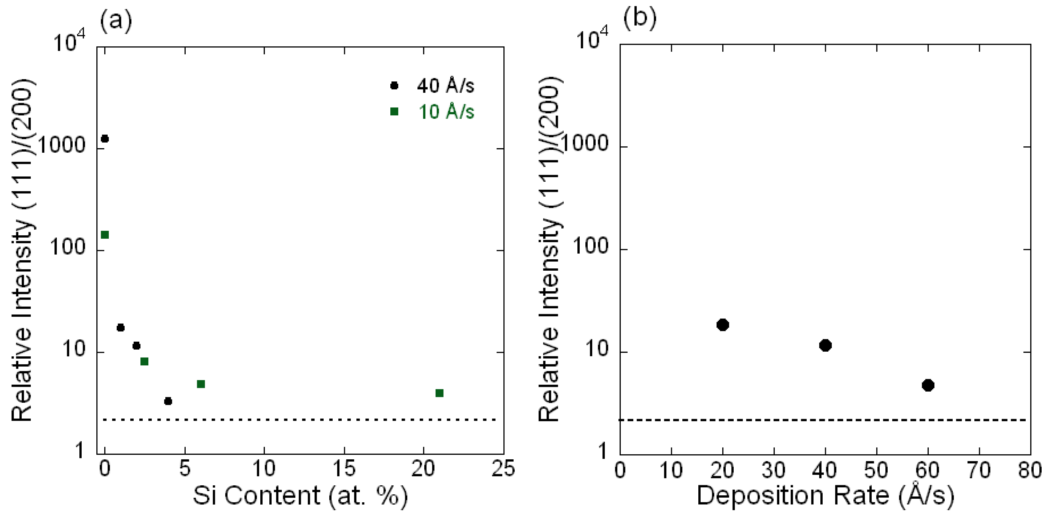

Figure 4.8: Changes in the intensity of the (111) Au diffraction peak relative to the (200) Au diffraction peak with (a) Si content in films deposited at 10 Å/s and 40 Å/s and (b) deposition rate for films containing 2 at. % Si. The dashed line represents the randomly oriented polycrystalline Au value [62]. Note that the vertical axis is on a logarithmic scale.

presented in Section 4.4. A decrease in average grain size is also observed to coincide with an increase in deposition rate.

Table 4.4: Average grain size of Au-Si films determined by XRD.

Film	W_{FWHM}	$d_{average}$
Au10Si0	0.192	46
Au10Si2.5	0.265	33
Au10Si6	0.335	26
Au10Si21	0.502	18
Au20Si2.5	0.244	36
Au40Si0	0.146	60
Au40Si1	0.268	33
Au40Si2	0.290	30
Au40Si4	0.324	27
Au60Si2	0.382	23

Additionally, plan view TEM was performed at CINT at LANL on the Au-Si films deposited at 10 Å/s. The remaining films have not been investigated by TEM. The resulting microstructure revealed the fine grain structure of films containing 0, 2.5, 6, and 21 at. % Si deposited at 10 Å/s shown in Figs. 4.9 (a)-(d), respectively.

It is clear when comparing Figs. 4.9 (a) and (b) that the addition of Si led to a decrease in grain size as compared with the pure Au film. Nanotwins were observed in each of the films deposited at 10 Å/s, with typical twin thicknesses on the order of several nanometers. A magnified image showing an example of a typical nanotwinned Au grain is shown in the inset of Fig. 4.9 (b). Si nanoparticles residing at the grain boundaries were observed in the TEM images of the 6 and 21 at. % Si films. A High Resolution TEM image of a Si particle is shown in the inset of Fig. 4.9 (c). Whereas the presence of Si was confirmed in the 2.5 at. % Si film by PIXE, no distinct Si particles could be observed in the TEM images. SAD was performed on each film to investigate the nature of the Si particles. The resulting patterns revealed the presence of the Au grains without any evidence of crystalline Si as shown in the inset of Fig. 4.9 (d), indicating that the particles were amorphous. In order to determine a representative grain size for these nanotwinned films, the minimum distance across each grain observed in a single TEM image was measured, where each twin was considered to be an individual grain. Table 4.5 summarizes the average Au grain size, Si particle size and Si

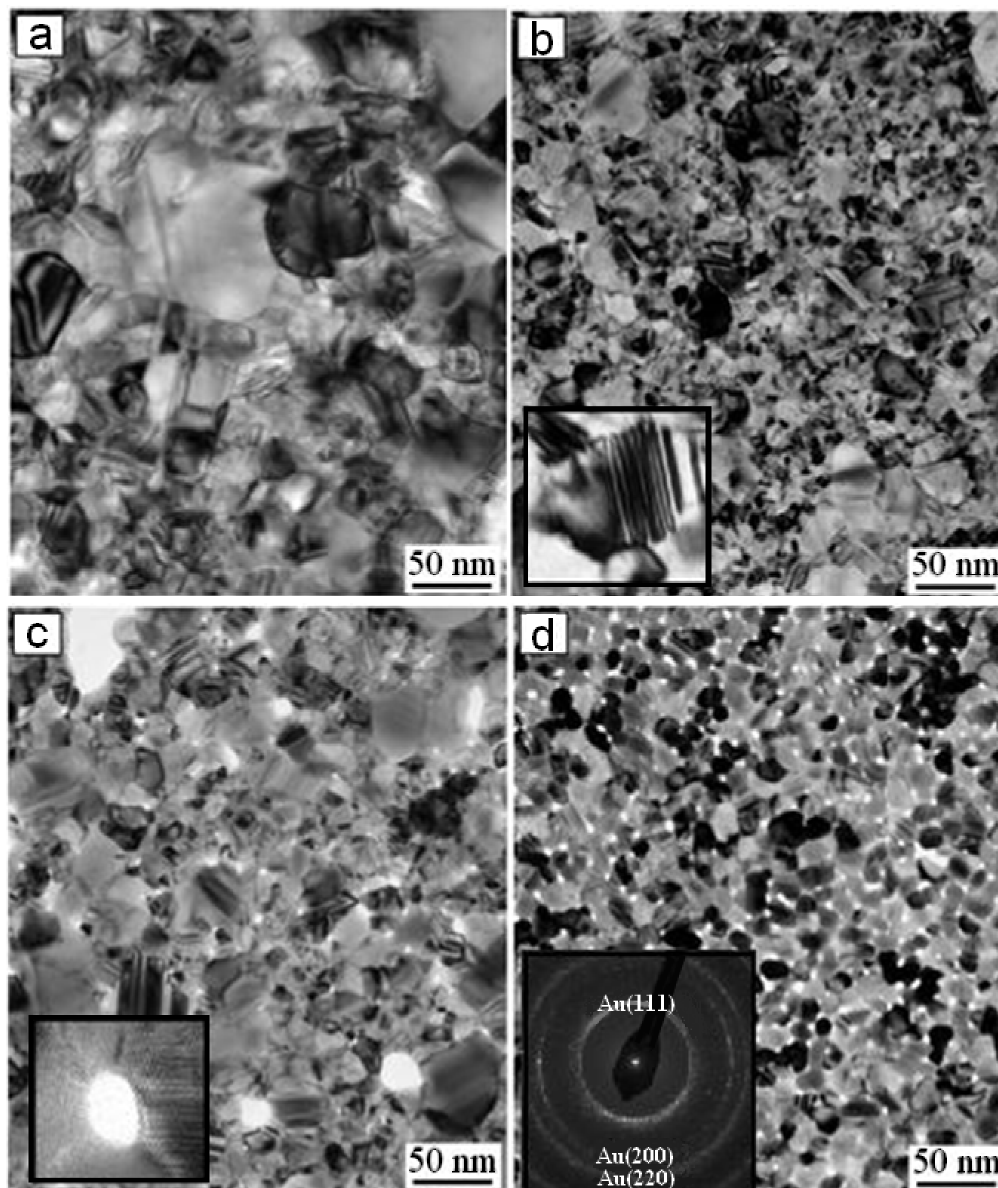

Figure 4.9: (a)-(d) Plan view TEM images of Au-Si films deposited at 10 Å/s containing 0, 2.5, 6, and 21 at. % Si, respectively. Inset dimensions are (b) 50 x 50 nm and (c) 20 x 20 nm

particle spacing observed for each film. The average minimum length of the Au grains appears to decrease with increasing Si content for films containing 0, 2.5 and 21 at. % Si, however the 6 at.% Si film does not follow this trend.

Table 4.5: Average minimum grain diameter of the Au-Si films deposited at 10 Å/s determined by TEM.

Film	Composition at. % Si	Au grain diameter (nm)	Si Particle Size (nm)	Si Particle Spacing (nm)
Au10Si0	0	15	-	-
Au10Si2.5	2.5	9	-	-
Au10Si6	6	15	6	40
Au10Si21	21	7	2	17

Grain sizes estimated by XRD are expected to overestimate the true grain size in these films, as the grains are likely to be columnar and XRD measures average grain depth normal to the surface. Conversely, the techniques used to calculate the grain size from the TEM measurements should underestimate the true grain size in these films, as the method of measuring the minimum grain diameter by definition selects the smallest possible measurement. In addition to this, the TEM measurements were taken on 30-50 nm thick films, and grain size has been shown to be a function of film thickness [17]. As TEM results are not available for all films, the grain size measured by XRD was used to compare the effects of Si content and deposition rate. The average grain size of films deposited at 10 Å/s was observed to decrease by about 25% from the pure Au film to the film containing 2.5 at. % Si. This is even more evident in the films deposited at 40 Å/s, where the grain size decreased from 60 nm for the pure Au film to 33 nm for the 1 at. % Si film. A plausible explination for this grain refinement is the Si particles, which are insoluble in Au, arrest Au grain growth during deposition [70]. Increasing deposition rate is also seen to cause a decrease in average grain size. Pashley [71] suggests that high deposition rates lead to less substrate heating due to shorter exposure to the high temperatures necessary for evaporation, therefore increasing deposition rates reduces the time for grain growth to occur. The (111) preferred orientation was observed to be more prevalent as deposition rate and Si content decreased, where conditions were more favorable for grain growth during deposition. As the (111) plane has the lowest surface energy for FCC metals [70], this orientation is more likely to grow as compared to the higher surface energy (200) and (220) planes. However, as the conditions become less favorable for grain growth, fewer of

the higher energy (200) and (220) oriented grains will coalesce with (111) oriented grains to form larger (111) oriented grains.

4.4 Mechanical properties

Nanoindentation was performed to investigate the mechanical properties of each film. Reported values are the average of five individual experiments at a contact depth of 100 nm, with the error bars representing the maximum and minimum results. Figures 4.10 shows the variation in hardness and reduced elastic modulus with Si content for films deposited at 10 Å/s and 40 Å/s. Hardness was observed to increase with Si content up to 6 at. % Si, but showed little improvement between 6 and 21 at. % Si. Observed increases in hardness with Si content correspond with the decreases in grain size observed in Table 4.4. The reduced elastic modulus was observed to decrease with increasing Si content. This decrease is consistent with the observed decrease in the relative intensity of the (111)/(200) Au diffraction peaks shown in Fig. 4.8, as the reduced elastic modulus for the (200) plane (50 GPa) is less than half that for the (111) plane (126 GPa) in Au [65]. Dashed lines representing the reduced elastic modulus values for the (111) and (200) planes in Au were plotted with the measured reduced elastic modulus values for comparison. In addition, an estimation of the reduced elastic modulus of randomly oriented polycrystalline Au is shown by the shaded region. The upper and lower bounds of this region were found using the Voigt and Reuss averages, respectively [65]. Voigt averaged the elastic stiffness over space, whereas Reuss averaged the elastic compliances [65].

The reduced elastic modulus of the 21 at. % Si film is lower than the polycrystalline estimation. This is not consistent with the XRD results, which indicated the film had a slight (111) preferred orientation. In order to be consistent, the measured reduced elastic modulus of the film should be approximately the same as the upper end of the polycrystalline estimate, similar to the reported value for the 6 at. % Si film. To investigate the cause of this low value, experiments were performed in multiple locations across the film. No variation in reduced elastic modulus was observed, which indicated the measured value was not caused by a variation in composition or structure across the film. Additionally, the effect of creep was considered as a possible source of error for this measurement. The load function used in this investigation was found not to satisfy the ISO guidelines that ensure the error due to creep was less than 1%. The relationship used to determine if the effect of creep could be significant is given as show in Eq. 4.4 [48].

$$(creep\,rate) \times (time\,to\,remove\,force) < F_{max} \times C_t/100 \tag{4.4}$$

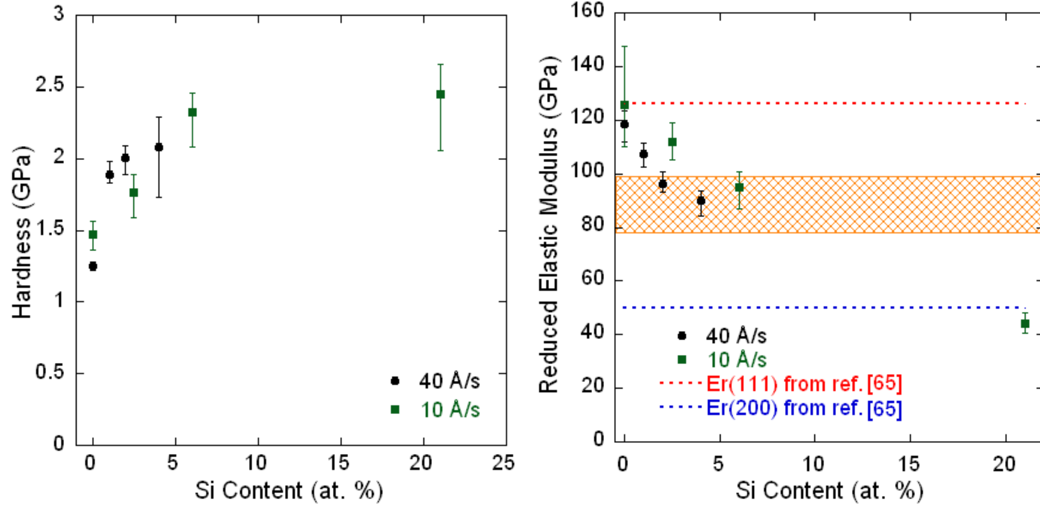

Figure 4.10: The effect of Si content on the hardness and reduced elastic modulus of Au-Si films deposited at 10 Å/s and 40 Å/s. The reduced elastic modulus plots show values for the (111) and (200) planes as dashed lines. The shaded region represents an estimation of the randomly oriented polycrystalline Au reduced elastic modulus based on the Voigt and Reuss averages.

In order to reduce the creep rate, the load rate was reduced and the hold time increased until the creep rate was minimized. The load function used to satisfy the ISO standard for reducing the error due to creep is shown in Fig. 4.11, where the load rate was reduced to 15 μN/s and the hold time was extended to 210 seconds. As the test time was much longer for these experiments, thermal drift rate was determined by the addition of a 60 second hold at 10% of the maximum load after the unload. The results of these experiments at a lower load rate and longer hold period showed no appreciable changes in reduced elastic modulus, which suggests that creep was not the cause of the lower reduced elastic modulus observed in the 21 at. % Si film. While the reduced elastic modulus of the 21 at. % Si film is not consistent with the XRD results, low modulus values have been previously reported for Au films [52, 72, 73]. Chasiotis et al. [52] and Long et al. [72] reported elastic modulus values of 30 to 40 GPa (corresponding to a reduced elastic modulus of 35 to 47 GPa), which is consistent with the measured reduced elastic modulus of the 21 at. % Si film. Haque and Saif [73] reported a measured elastic modulus of 52 GPa (corresponding to a reduced elastic modulus of 58 GPa) for a film with an average grain size of 15 nm, whereas another film with an average grain size of 75 nm had a measured elastic modulus closer to that of bulk Au. They suggest the lower modulus could be due to some grain boundary compliance, which becomes evident at low grain sizes [73].

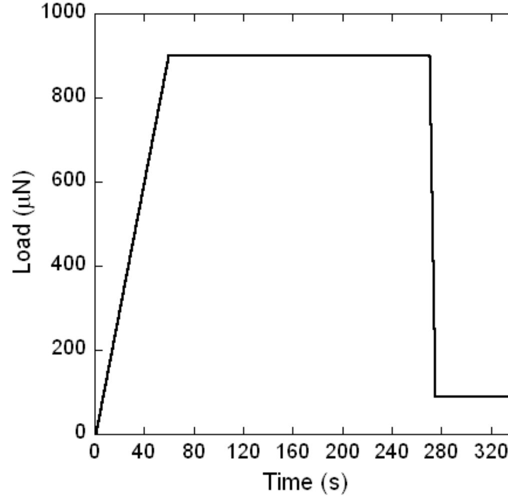

Figure 4.11: The load function used to minimize creep in the 21 at. % Si film.

The grain size of the 21 at. % Si film in this study as measured by XRD was 18 nm, which is similar to the film investigated by Haque and Saif [73]. Additionally, the modulus of the 21 at. % Si film in this study would be expected to be lower than that of the pure Au film investigated by Haque and Saif [73], as pure Au films showed a strong (111) preferred orientation which corresponded to higher values of reduced elastic modulus compared with films containing Si.

Figure 4.12 shows the variation in hardness and reduced elastic modulus with deposition rate for 2 at. % Si films. The trend of hardness with deposition rate was unclear, however it appears similar to the trend observed in the electrical resistivity reported in Section 4.6. The reduced elastic modulus was not observed to change with deposition rate.

Surface roughness was one source of error in these nanoindentation experiments, because it caused differences between the calculated contact area and actual contact area, as described in Section 2.3.1. Figure 4.13 shows the variation of hardness measurements over a range of applied loads on the pure Au film. Nine load controlled experiments were performed at each load in order to more clearly show the variation in hardness at a fixed load. The slope of the curve traced by each set of data points is steepest at the lowest contact depths, and becomes less severe as the contact depth increases, consistent with Eq. 2.6 where hardness varies as $P_{max}/A(h_c)$. When the load, P_{max} is constant the hardness results vary as $1/A(h_c)$. The ideal area function for a Berkovich tip is 24.5 h_c^2, so the measured hardness follows a trend that is approximately $1/h_c^2$. At a given load, the variation observed must be interpreted into a representative hardness in order to compare results from different films.

The variation in contact depth over five measurements for each of the films was compared to the

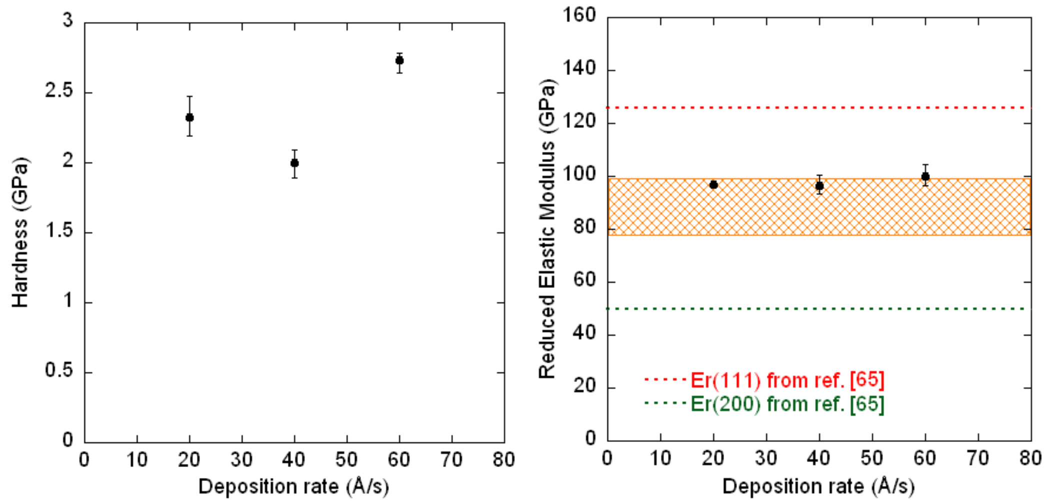

Figure 4.12: The effect of deposition rate on the hardness and reduced elastic modulus of Au-Si films containing 2 at. % Si. The reduced elastic modulus plots show values for the (111) and (200) planes as dashed lines. The shaded region represents an estimation of the randomly oriented polycrystalline Au reduced elastic modulus based on the Voigt and Reuss averages.

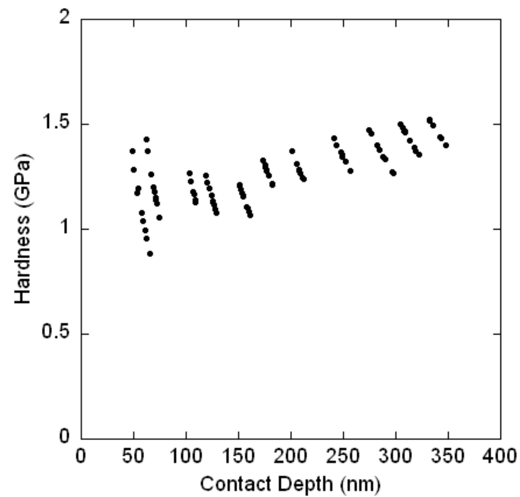

Figure 4.13: The variation in measured hardness of a pure Au film over a range of contact depths.

measured surface roughness as shown in Fig. 4.14, where the variation in contact depth is on the x axis and the average surface roughness (Ra) is on the y axis. The figure shows good correlation between the variation observed in the nanoindentation results and the average surface roughness measurements obtained by AFM, indicating that surface roughness is responsible for the observed variation in hardness in load controlled nanoindentation experiments.

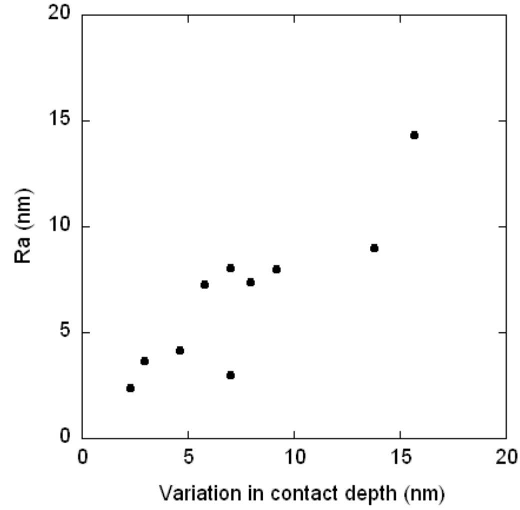

Figure 4.14: The correlation between the variation in contact depth at a set load for each Au-Si film with the average surface roughness as measured by AFM.

4.5 Strengthening mechanisms

In order to understand the strength of these Au-Si films, it was necessary to determine what mechanisms are responsible for the increase in strength observed by nanoindentation. An understanding of the factors that affect the strength of these films should enable the mechanical strength to be predicted based on the structure of the film. The grain size was observed to decrease with increasing strength, which suggested that the Hall-Petch relation could describe the strength of these films. Using the measured grain sizes shown in Table 4.4, the strength of the film can be estimated by the Hall-Petch relation [8], given by

$$\sigma_0 = \sigma_i + kD^{-1/2} \tag{4.5}$$

where σ_i is the friction stress, k is the locking parameter, and D is the grain size in nm. The constants σ_i and k were determined from a linear fit of experimental data shown in Fig. 4.15, which was compiled from studies of pure Au films with a range of grain sizes from 21 nm to 130 μm [16–20, 26]. These studies utilized films synthesized by a variety of techniques (sputtering [16, 19], compressed

porous foam [20], electrodeposition [26], electron beam evaporation [18, 19]) where the mechanical strength was measured by a variety of testing methods (indentation [16, 17, 20, 26], micro-tensile test [19], micro cantilever beam bending [18]). Based on the compiled results, the values for σ_i and k for Au films were then estimated to be 152 MPa and 1,998 MPa/nm$^{1/2}$, respectively. While Dieter [8] suggests that caution must be used when the Hall-Petch relation is applied to very small grain sizes, experimental studies on Au-Cu films have observed the strength of these films to follow the Hall-Petch relation down to grain sizes of 6 nm [32] and 3 nm [18].

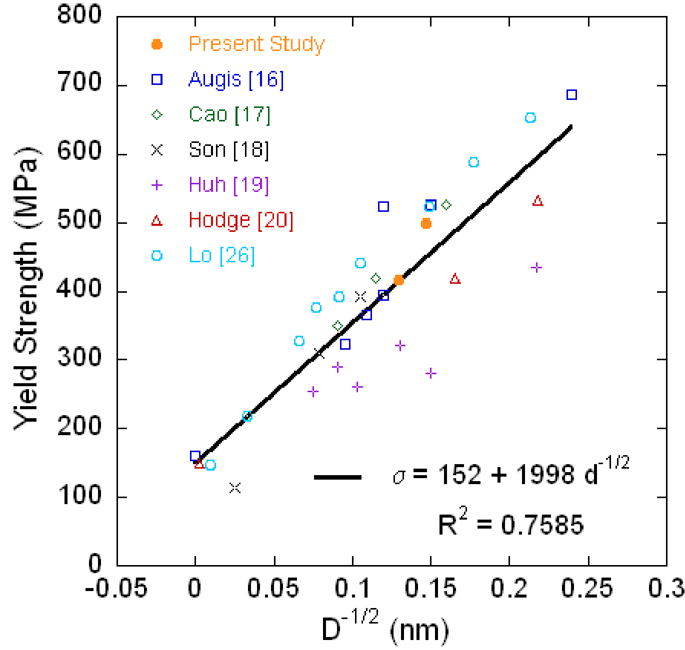

Figure 4.15: Hall-Petch plot of hardness as a function of average grain diameter compiled from experiments from the literature conducted on pure Au films.

In addition to the refined grain structure, amorphous Si particles were observed in the TEM images of films deposited at 10 Å/s containing 6 and 21 at. % Si. To account for the effect of these Si particles on the strength of the films, the Orowan-Ashby relationship was utilized [8]

$$\delta\sigma_{orowan} = \frac{0.13Gb}{\lambda} ln(\frac{r}{b}) \tag{4.6}$$

where $\delta\sigma_{orowan}$ is the increase in predicted strength due to the particles, G is the shear modulus, b is the Burgers vector, λ is the spacing between particles, and r is the radius of the particles. The shear modulus was calculated by $G = \frac{E}{2(1+\nu)}$ where E and ν were taken to be 78.5 GPa and 0.42 [74], respectively. The Burgers vector was approximated as the (111) atomic spacing of Au

(0.29 nm) [62], and values for λ and r are shown in Table 4.5. The calculated increase in strength due to the presence of Si particles was found to be 78 and 129 MPa for the 6 and 21 at. % Si films deposited at 10 Å/s, respectively.

In order to compare the predicted strength to the measured hardness, the Tabor relation [75] $H = 3\sigma$, was used. The variation of measured and predicted hardness with Si content for films deposited at 10 Å/s is shown in Fig. 4.16. Error bars on the measured hardness represent the maximum and minimum values for five experiments. The predicted hardness of each film was estimated using the Hall-Petch relation (Eq. 4.5) with the average grain size determined by XRD. Predictions based on the average minimum grain diameter determined from the TEM images are also shown. Additionally, Orowan strengthening due to the ability of fine particles to block dislocation movement was considered for both the 6 and 21 at. % Si films as Si particles were observed in the TEM images. The contribution from Orowan strengthening was added to the prediction based on the Hall-Petch prediction determined from the average minimum diameter. The predicted hardness based on XRD grain size for the pure Au film agrees well with the measured value, however the predicted hardness of the films containing Si underestimated the measured value. One possible explanation for the underestimation of the film hardness is formation of fine Si particles at grain boundaries during deposition. The average grain size calculated from the XRD results is a measure of the depth of regions of a particular crystal structure, with no regard to the lateral dimensions. Si is immiscible in Au, and has been observed to form particles at the grain boundaries in Au-Si films in Fig. 4.9. Columnar grain growth is well documented in the literature for thin films of pure metals, including Au [37, 67–69]. These particles could prevent the grains from growing laterally, further encouraging columnar grain growth of many individual grains. This would make the assumption of equiaxed grains used to calculate the average grain size from the XRD results incorrect, leading to an overestimation of the average grain size by XRD. The difference between the measured and predicted hardness does not appear to increase with increasing Si content, suggesting that a relatively small amount of Si results in this refined lateral grain structure. Similarly, Fig. 4.17 shows good agreement between the predicted hardness of films deposited at 40 Å/s based on the XRD grain size estimations and the measured hardness for the pure Au film, whereas the predicted hardness of films containing Si underestimated the measured value. No predictions based on TEM grain size or Orowan strengthening were presented as TEM was not performed on these films. Figure 4.18 shows the measured and predicted hardness plotted against deposition rate for films containing 2 at. % Si. Despite a decrease in grain size determined by XRD, there is no evidence that increasing the deposition rate causes any measurable change in the lateral grain size.

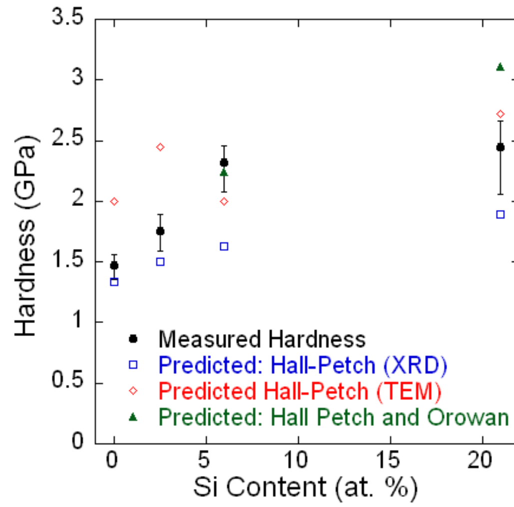

Figure 4.16: Measured and predicted hardness of Au-Si films deposited at 10 Å/s. Error bars on the experimental data represent the observed maximum and minimum values of five measurements. The predicted hardness values are based on the Hall-Petch relation with grain sizes determined by both XRD and TEM, as well as the combination of grain size (TEM) and Orowan strengthening.

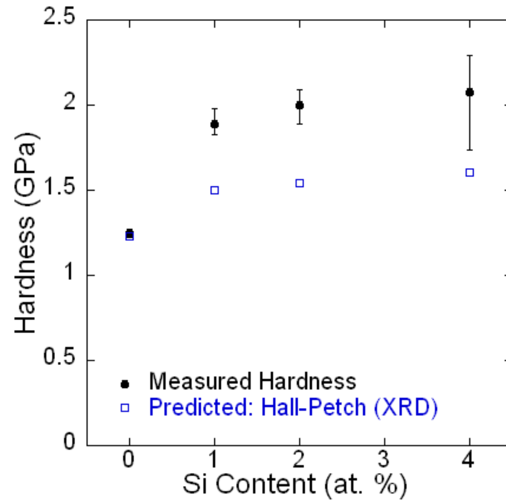

Figure 4.17: Measured and predicted hardness of Au-Si films deposited at 40 Å/s. Error bars on the experimental data represent the observed maximum and minimum values of five measurements. The predicted hardness is based on the Hall-Petch relation.

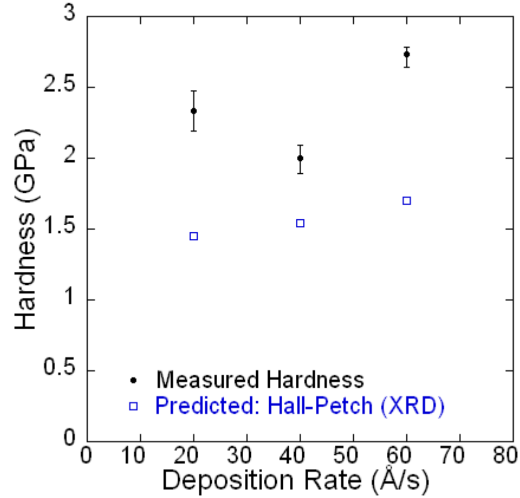

Figure 4.18: Measured and predicted hardness of Au-Si films containing 2 at. % Si. Error bars on the experimental data represent the observed maximum and minimum values of five measurements. The predicted hardness is based on the Hall-Petch relation.

As discussed previously, grain sizes estimated by XRD are expected to overestimate the true grain size, as the grains are likely to be columnar and XRD measures average grain depth normal to the film. This would explain the underestimation of the film hardness observed in Figs. 4.16 and 4.17. Conversely, the TEM measurements should underestimate the true grain size in these films, as the method of measuring the minimum grain diameter by definition selects the smallest possible measurement. This explains the overestimation of the hardness observed in Fig. 4.16. The predictions for the 6 at. % film do not reflect this trend, however the average minimum length for this film was higher compared with the 2.5 and 21 at. % films. The cause of this is unclear, however the agreement between the experimental data and the predicted hardness suggests that the effects of grain size and particle dispersion on the strength of these Au-Si films can be described by the combination of the Hall-Petch relation and Orowan strengthening.

4.6 Electrical properties

Four point resistivity probe measurements were performed to investigate the electrical properties of each film. Reported values are the average of four individual experiments, where each film was rotated 90° between experiments. Figures 4.19 (a)-(b) show the variation in resistivity with Si content for films deposited at 10 Å/s and 40 Å/s respectively, and Fig. 4.19 (c) shows the variation in resistivity with deposition rate for films containing 2.5 vol. % Si. The resistivity is seen to increase

with Si content. The trend of resistivity with deposition rate is not clear, however it appears similar to the trend of hardness with deposition rate shown in Fig. 4.12.

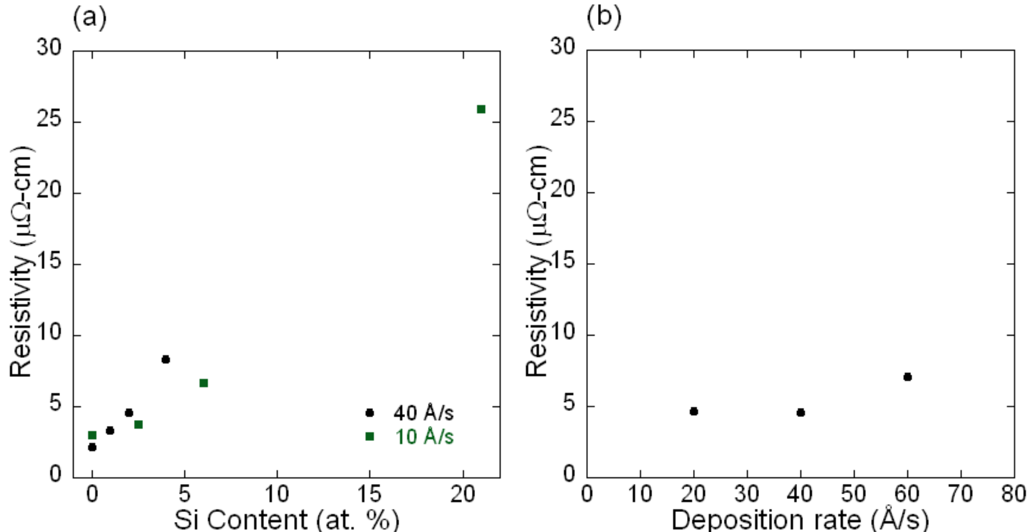

Figure 4.19: Resistivity of Au-Si films as a function of (a) Si content in films deposited at 10 Å/s and 40 Å/s and (b) deposition rate for films containing 2 at. % Si. The maximum and minimum of four measurements were within 0.06 $\mu\Omega$-cm or less of the average.

Resistivity is known to follow Matthiessen's rule, where the total resistivity ρ_{total} is the sum of the contributions from thermal vibrations ρ_t, impurities ρ_i and lattice defects ρ_d. As all the measurements were taken at room temperature, the thermal contribution should be the same for all the films, which means that the differences observed between these films are due to lattice defects and impurities. Figure 4.19 (a) illustrates the effect of the intentionally co-deposited Si impurities on the resistivity of the films. The observed increase in resistivity in films containing 2 at. % Si deposited at 20, 40, and 60 Å/s shown in Fig. 4.19 (b) can be attributed to the decrease in grain size determined by XRD, shown in Table 4.4, as the effect of Si content on the resistivity was the same for these films.

The mean free path of electrons in Au is reported to be 38 nm [76]. Each of the Au-Si films in the current study exhibit a high degree of electron scattering due to their fine grained structure. The refined grain structure has also been shown to be the cause of the increased strength observed in these films. Nanotwins have been shown to have the same ability to block dislocations as grain boundaries [36], which is consistent with Dieter [8]. However, Anderoglu et al. [34] have found that twin boundaries create an order of magnitude less electron scattering than grain boundaries, which suggests that nanotwinned films would be comparable in strength to a nanocrystalline film without

the increase in resistivity due to electron scattering at high-angle grain boundaries. Figure 4.20 shows a comparison of the films from the present study with four other studies of Au films that were strengthened by particle dispersion [40,41,44] and nanolayering [12]. It can be seen that all the data presented in this plot follows the general trend of decreasing electrical conductivity with increasing strength. For the films investigated in this study, the plot suggests that increasing the Si content past 4 at. % Si is not desirable for the creation of a high-strength film for electrical contacts, as the conductivity decreases continuously while the strength does not improve significantly. While the pure Au film deposited at 40 Å/s (Au40Si0) has the highest conductivity, the 1 at. % Si film deposited at 40 Å/s (Au40Si1) shows the most efficient increase in strength with regards to the impact on conductivity. The objective of increasing the deposition rate was to increase the strength of the Au-Si films by twinning instead of grain refinement, in order to create films with increased strength and high conductivity compared to nanocrystalline Au films. However the decrease in conductivity with deposition rate shown in Fig. 4.20 suggests that any increases in twinning with deposition rate were negligible compared to the increase in high angle grain boundaries. If a technique could be developed to synthesize Au films with different twin densities, the result would be expected to follow the new trend listed in Fig. 4.20.

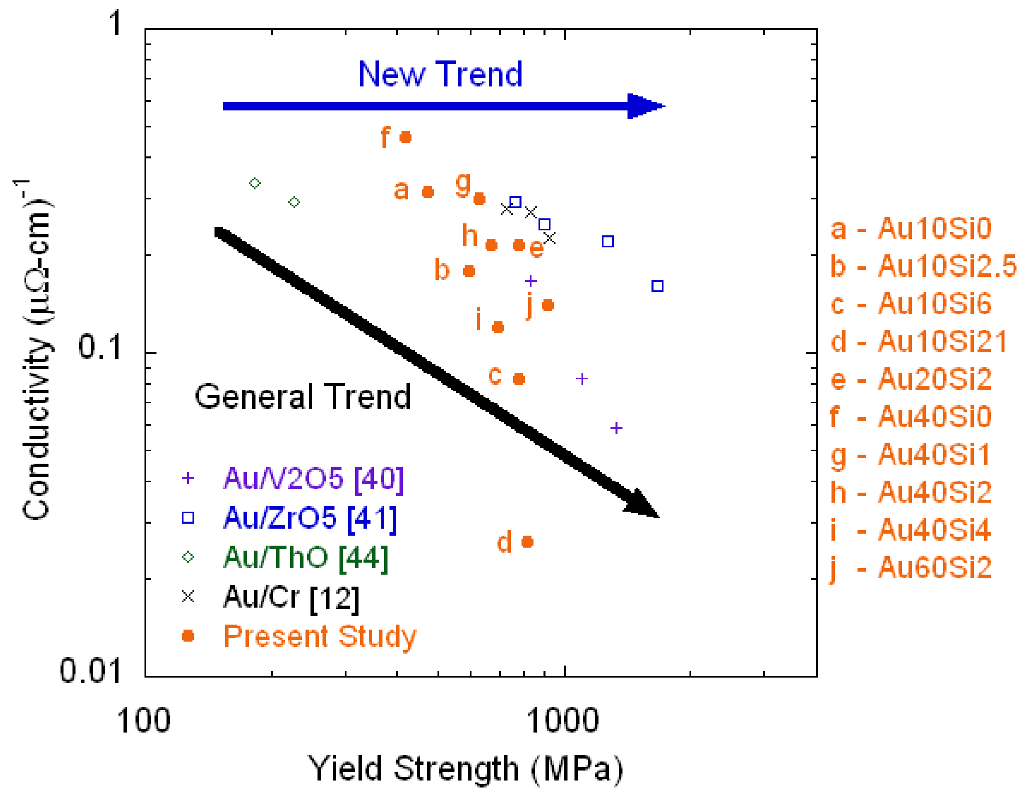

Figure 4.20: The general trend of electrical conductivity with yield strength and the new trend to increase strength while maintaining electrical conductivity for strengthened Au films.

Chapter 5

Conclusions and future work

5.1 Conclusions

A study of the mechanical strength of nanocrystalline Au-Si films has been performed. The increase in mechanical strength measured by nanoindentation was found to correspond to an observed decrease in grain size, as well as the presence of amorphous Si nanoparticles at Au grain boundaries for some films. The addition of Si was found to correspond to a decrease in average Au grain size relative to pure Au films. Average Au grain size was also observed to decrease with increasing deposition rate, and nanotwinned Au grains were observed in all films investigated by TEM. These observations led to the conclusion that the increase in mechanical strength in these Au-Si films could be described by a combination of Hall-Petch and Orowan strengthening mechanisms. The following are specific conclusions resulting from this investigation.

1. Surface roughness measured by AFM was observed to increase with Si content and decrease with deposition rate.

2. Nanotwinned Au grains were observed in the TEM images of the films deposited at 10 Å/s. In addition, Si nanoparticles were observed at the grain boundaries in the films containing 6 and 21 at. % Si deposited at 10 Å/s. The particles were determined to be amorphous due to their lack of diffraction in either SAD or XRD. Grain size was determined by XRD for all films, and was observed to decrease with increasing Si content. This is thought to be caused by the Si particles, which are insoluble in Au, arresting Au grain growth. Increasing deposition rate was also observed to decrease the grain size, which is thought to be caused by the reduction in time at elevated deposition temperatures.

3. Reduced elastic modulus was observed to decrease with increasing Si content for films deposited at 10 Å/s and 40 Å/s. This is consistent with the observed shift in the preffered orientation of the film from the (111) plane toward the (200) plane, as the reduced elastic modulus of the (200) plane in Au is less than half that of (111) plane. A plausible explanation for this shift is the Si particles arresting Au grain growth during deposition, resulting in more randomly oriented Au grain structure.

4. The reduced elastic modulus of the film deposited at 10 Å/s with a Si content of 21 at. % was lower than expected based on the XRD results. The values were found to be consistent accross the surface of the film, and reducing the effects of creep was determined to have no effect on the reduced elastic modulus of this film. However, low modulus values for Au films have been previously reported in the literature.

5. The hardness of the films was observed to increase with increasing Si content. Increases in measured hardness were shown to be described by a combination of the Hall-Petch relationship and Orowan strengthening. Grain size estimations from the XRD results were shown to underestimate the strength of the films, which indicates the grains are columnar in nature. Conversely grain size estimates from the plan view TEM were shown to overestimate the film strength, which may be due to the 30-50 nm thick films having a smaller grain size than the 1 μm thick films investigated by nanoindentation.

6. Resistivity was observed to increase linearly with Si content.

5.2 Future Work

1. Perform PIXE and plan view TEM on films deposited at deposition rates higher than 10 Å/s to further investigate the composition and structure of these films. TEM specimens should be fabricated by focused ion beam milling from the 1 μm thick films used for all other measurements in this study. Milling the specimens directly from the 1 μm thick films will allow images of the microstructure present in the films investigated in the previous experiments directly, rather than a thinner film which might show a smaller grain size due to the relationship between grain size and film thickness.

2. Perform cross sectional TEM to investigate the structure of the films as a function of depth, as well as confirm or deny the presence of columnar Au grains.

3. Perform a more expansive study of Pure Au and 1 at. % Si films with a wide range of deposition rates to more thoroughly investigate the effect of deposition rate on grain size, mechanical strength, and resistivity.
4. Investigate methods to increase the twin density and decrease twin spacing in these films without increasing Si content in order to increase mechanical strength and maintain electrical resistivity.
5. Explore the effects of heat treatment on the microstructure, mechanical strength, and electrical resistivity of these Au-Si films.

Bibliography

[1] G. Rebeiz, "RF MEMS switches: Status of the technology," in *TRANSDUCERS,12th International Conference on Solid-State Sensors, Actuators and Microsystems*, vol. 2, pp. 1726 – 1729, 2003.

[2] S. Majumder, N. McGruer, G. Adams, P. Zavracky, R. Morrison, and J. Krim, "Study of contacts in an electrostatically actuated microswitch," *Sensors and Actuators A: Physical*, vol. 93, pp. 19 – 26, 2001.

[3] B. Dvorak, *Investigation of the near surface mechanical properties of* Au – Si *thin films*. Master's thesis, Oklahoma State University, 2008.

[4] R. C. Jr., P. Kladitis, K. Leedy, and R. Crane, "Selecting metal alloy electric contact materials for mems switches," *Journal of Micromechanics and Microengineering*, vol. 14, p. 1157, 2004.

[5] B. Arrazat, V. Mandrillon, K. Inal, M. Vincent, and C. Poulain, "Microstructure evolution of gold thin films under spherical indentation for micro switch contact applications," *Journal of Materials Science*, vol. 46, pp. 6111–6117, 2011.

[6] S. Patton and J. Zabinski, "Fundamental studies of Au contacts in MEMS RF switches," *Tribology Letters*, vol. 18, pp. 215–230, 2005.

[7] D. Hyman and M. Mehregany, "Contact physics of gold microcontacts for mems switches," *IEEE Transactions on Components and Packaging Technologies*, vol. 22, pp. 357 –364, 1999.

[8] G. Dieter, *Mechanical Metallurgy*. Boston: McGraw Hill, 3rd edition ed., 1986.

[9] J. McBride, E. Yunus, and S. Spearing, "Gold coated carbon nanotube surfaces as low force electrical contacts for MEMS devices: Part 1," *55th IEEE Holm Conference on Electrical Contacts*, 2009.

[10] H. Lee, R. Coutu, S. Mall, and K. Leedy, "Characterization of metal and metal alloy films as contact materials in MEMS switches," *Journal of Micromechanics and Microengineering*, vol. 16, pp. 557–563, 2006.

[11] G. Jahromi, *Investigation of the near surface mechanical properties of* Au − Ti *thin films*. Master's thesis, Oklahoma State University, 2008.

[12] V. Mulloni, R. Bartali, S. Colpo, F. Giacomozzi, N. Laidani, and B. Margesin, "Electrical and mechanical properties of layered gold chromium thin films for ohmic contacts in RF-MEMS switches," *Materials Science and Engineering: B*, vol. 163, pp. 199 – 203, 2009.

[13] N. Togasaki, Y. Okinaka, T. Homma, and T. Osaka, "Preparation and characterization of electroplated amorphous gold nickel alloy film for electrical contact applications," *Electrochimica Acta*, vol. 51, pp. 882 – 887, 2005.

[14] M. Adamov, B. Perovic, and T. Nenadovic, "Electrical and structural properties of thin gold films obtained by vacuum evaporation and sputtering," *Thin Solid Films*, vol. 24, pp. 89–100, 1974.

[15] D. Pashley, "A study of the deformation and fracture of single-crystal gold films of high strength inside an electron microscope," *Proceedings of the Royal Society of London. Series A, Mathematical and Physical Sciences*, vol. 255, pp. 218–231, 1960.

[16] J. Augis, C. Lo, and M. Pinnel, "The hardness and ductility of sputtered gold films," *Thin Solid Films*, vol. 58, pp. 357 – 363, 1979.

[17] Y. Cao, S. Allameh, D. Nankivil, S. Sethiaraj, T. Otiti, and W. Soboyejo, "Nanoindentation measurements of the mechanical properties of polycrystalline Au and Ag thin films on silicon substrates: Effects of grain size and film thickness," *Materials Science and Engineering: A*, vol. 427, pp. 232 – 240, 2006.

[18] D. Son, J. Jeong, and D. Kwon, "Film-thickness considerations in microcantilever-beam test in measuring mechanical properties of metal thin film," *Thin Solid Films*, vol. 437, pp. 182 – 187, 2003.

[19] Y.-H. Huh, D.-I. Kim, D.-J. Kim, H.-M. Lee, and J.-H. Park, "Dependency of micro-mechanical properties of gold thin films on grain size," in *Engineering Against Fracture* (S. Pantelakis and C. Rodopoulos, eds.), pp. 339–346, Springer Netherlands, 2009.

[20] A. M. Hodge, J. Biener, L. L. Hsiung, Y. M. Wang, A. V. Hamza, and J. H. Satcher, "Monolithic nanocrystalline Au fabricated by the compaction of nanoscale foam," *Journal of Materials Research*, vol. 20, pp. 554–557, 2005.

[21] Y. Chew, C. Wong, F. Wulff, F. Lim, and H. Goh, "Strain rate sensitivity and Hall-Petch behavior of ultrafine-grained gold wires," *Thin Solid Films*, vol. 516, pp. 5376 – 5380, 2008.

[22] M. Dietiker, R. Nyilas, C. Solenthaler, and R. Spolenak, "Nanoindentation of single-crystalline gold thin films: Correlating hardness and the onset of plasticity," *Acta Materialia*, vol. 56, pp. 3887 – 3899, 2008.

[23] R. Emery and G. Povirk, "Tensile behavior of free-standing gold films. Part I. Coarse-grained films," *Acta Materialia*, vol. 51, pp. 2067 – 2078, 2003.

[24] R. Emery and G. Povirk, "Tensile behavior of free-standing gold films. Part II. Fine-grained films," *Acta Materialia*, vol. 51, pp. 2079 – 2087, 2003.

[25] S. Sakai, H. Tanimoto, and H. Mizubayashi, "Mechanical behavior of high-density nanocrystalline gold prepared by gas deposition method," *Acta Materialia*, vol. 47, pp. 211 – 217, 1998.

[26] C. Lo, J. Augis, and M. Pinnel, "Hardening mechanisms of hard gold," *Journal of Applied Physics*, vol. 50, pp. 6887–6891, 1979.

[27] R. W. Armstrong, Y. T. Chou, R. M. Fisher, and N. Louat, "The limiting grain size dependence of the strength of a polycrystalline aggregate," *Philosophical Magazine*, vol. 14, pp. 943–951, 1966.

[28] C. Koch and J. Narayan, "The inverse Hall-Petch effect- fact or artifact?," *Materials Research Symposium*, vol. 634, pp. B5.1.1–11, 2001.

[29] C. Carlton and P. Ferreira, "What is behind the inverse Hall-Petch effect in nanocrystalline materials?," *Acta Materialia*, vol. 55, pp. 3749 – 3756, 2007.

[30] J. Trelewicz and C. Schuh, "The Hall-Petch breakdown in nanocrystalline metals: A crossover to glass-like deformation," *Acta Materialia*, vol. 55, pp. 5948 – 5958, 2007.

[31] M. Zhao, J. Li, and Q. Jiang, "Hall-Petch relationship in nanometer size range," *Journal of Alloys and Compounds*, vol. 361, pp. 160 – 164, 2003.

[32] E. Brun, F. Durut, R. Botrel, M. Theobald, O. Legaie, I. Popa, and V. Vignal, "Influence of the electrochemical parameters on the properties of electroplated $Au - Cu$ alloys," *Journal of The Electrochemical Society*, vol. 158, pp. D223–D227, 2011.

[33] Y. Wang, A. Jankowski, and A. Hamza, "Strength and thermal stability of nanocrystalline gold alloys," *Scripta Materialia*, vol. 57, pp. 301 – 304, 2007.

[34] O. Anderoglu, A. Misra, F. Ronning, H. Wang, and X. Zhang, "Significant enhancement of the strength-to-resistivity ratio by nanotwins in epitaxial Cu films," *Journal of Applied Physics*, vol. 106, p. 024313, 2009.

[35] L. Lu, Y. Shen, X. Chen, L. Qian, and K. Lu, "Ultrahigh strength and high electrical conductivity in copper," *Science*, vol. 304, pp. 422–426, 2004.

[36] M. Merz and S. Dahlgren, "Tensile strength and work hardening of ultrafine-grained high-purity copper," *Journal of Applied Physics*, vol. 46, pp. 3235–3237, 1975.

[37] X. Zhang, H. Wang, X. Chen, L. Lu, K. Lu, R. Hoagland, and A. Misra, "High-strength sputter-deposited Cu foils with preferred orientation of nanoscale growth twins," *Applied Physics Letters*, vol. 88, p. 173116, 2006.

[38] M. Bernardi, S. Raja, and S. Lim, "Nanotwinned gold nanowires obtained by chemical synthesis," *Nanotechnology*, vol. 21, p. 285607, 2010.

[39] O. Anderoglu, A. Misra, H. Wang, and X. Zhang, "Thermal stability of sputtered Cu films with nanoscale growth twins," *Journal of Applied Physics*, vol. 103, p. 094322, 2008.

[40] T. Bannuru, W. Brown, S. Narksitipan, and R. Vinci, "The electrical and mechanical properties of $Au - V$ and $Au - V_2O_5$ thin films for wear-resistant RF MEMS switches," *Journal of Applied Physics*, vol. 103, p. 083522, 2008.

[41] J. Williams and D. Clarke, "Strengthening gold thin films with zirconia nanoparticles for MEMS electrical contacts," *Acta Materialia*, vol. 56, pp. 1813 – 1819, 2008.

[42] J. Williams, *Nano-dispersion strengthened gold films for MEMS electrical contacts.* Ph.D. Dissertation, University of California Santa Barbara, 2008.

[43] T. Chudoba, P. Schwaller, R. Rabe, J.-M. Breguet, and J. Michler, "Comparison of nanoindentation results obtained with berkovich and cube-corner indenters," *Philosophical Magazine*, vol. 86, pp. 5265–5283, 2006.

[44] N. Fuschillo and M. L. Gimpl, "Electrical and tensile properties of $Cu-ThO_2$, $Au-ThO_2$, $Pt-ThO_2$; and $Au-Al_2O_3$, $Pt-Al_2O_3$ alloys," *Journal of Materials Science*, vol. 5, pp. 1078–1086, 1970.

[45] R. P. Anantatmula, A. A. Johnson, S. P. Gupta, and R. J. Horylev, "The gold-silicon phase diagram," *Journal of Electronic Materials*, vol. 4, pp. 447–463, 1974.

[46] N. Dhere and C. Loural, "Metastable structures in $Au-Si$ thin films," *Thin Solid Films*, vol. 81, pp. 213 – 223, 1981.

[47] W. Robison, R. Sharma, and L. Eyring, "Observation of gold-silicon alloy formation in thin films by high resolution electron microscopy," *Acta Metallurgica et Materialia*, vol. 39, pp. 179 – 186, 1991.

[48] "ISO 14577-Metallic materials-Instrumented indentation test for hardness and materials parameters," *International Organization for Standardization*, vol. Geneva, Switzerland, ISO 14577 1-4, 2002.

[49] W. Oliver and G. Pharr, "An improved technique for determining hardness and elastic modulus using load and displacement sensing indentation experiments," *Journal of Material Research*, vol. 7, pp. 1564–1583, 1992.

[50] D. Lucca, K. Herrmann, and M. Klopfstein, "Nanoindentation: Measuring methods and applications," *CIRP Annals Manufacturing Technology*, vol. 59, pp. 803–819, 2010.

[51] *Hysitron Inc. Triboindenter® User Manual.* 2005.

[52] I. Chasiotis, C. Bateson, K. Timpano, A. McCarty, N. Barker, and J. Stanec, "Strain rate effects on the mechanical behavior of nanocrystalline Au films," *Thin Solid Films*, vol. 515, pp. 3183 – 3189, 2007.

[53] K. Jonnalagadda, N. Karanjgaokar, I. Chasiotis, J. Chee, and D. Peroulis, "Strain rate sensitivity of nanocrystalline au films at room temperature," *Acta Materialia*, vol. 58, pp. 4674 – 4684, 2010.

[54] G. Pharr, E. Herbert, and Y. Gao, "The Indentation Size Effect: A Critical Examination of Experimental Observations and Mechanistic Interpretations," *Annual Review of Materials Science*, vol. 40, pp. 271–292, 2010.

[55] T. Connolley, P. McHugh, and M. Bruzzi, "A review of deformation and fatigue of metals at small size scales," *Fatigue and Fracture of Engineering Materials and Structures*, vol. 28, pp. 1119–1152, 2005.

[56] W. Nix and H. Gao, "Indentation size effects in crystalline materials: A law for strain gradient plasticity," *Journal of Mechanics Physics of Solids*, vol. 46, pp. 411–425, 1998.

[57] S. Chakravarthy and W. Curtin, "Stress-gradient plasticity," *Proceedings of the National Academy of Science*, vol. 108, pp. 15716–15720, 2011.

[58] A. Elmustafa, J. Eastman, M. Rittner, J. Weertman, and D. Stone, "Indentation size effect: large grained aluminum versus nanocrystalline aluminum-zirconium alloys," *Scripta Materialia*, vol. 43, pp. 951 – 955, 2000.

[59] E. Lilleodden and W. Nix, "Microstructural length-scale effects in the nanoindentation behavior of thin gold films," *Acta Materialia*, vol. 54, pp. 1583 – 1593, 2006.

[60] A. Krawitz, *Introduction to Diffraction in Materials Science and Engineering*. New York: John Wiley and Sons, 2001.

[61] F. Smits, "Measurement of sheet resistivities with the four-point probe," *The Bell System Technical Journal*, vol. 37, pp. 711–718, 1958.

[62] R. Downs and M. Hall-Wallace, "The American Mineralogist crystal structure database," *American Mineralogist*, vol. 88, no. 1, pp. 247–250, January 2003.

[63] V. Inc., *FPP-5000 Four Point Resistivity Probe Installation, Operation and Maintenance Manual*. Santa Barbara: Sloan Technology (Veeco Instruments Inc.

[64] B. Agarwal, L. Broutman, and K. Chandrashekhara, *Analysis and Performance of Fiber Composites*. Hoboken: John Wiley and Sons, 3rd edition ed., 2006.

[65] G. Simmons and H. Wang, *Single Crystal Elastic Constants and Calculated Aggregate Properties: A Handbook*. Cambridge: The M.I.T. Press, 2nd ed., 1971.

[66] J. S. Custer, M. O. Thompson, D. C. Jacobson, J. M. Poate, S. Roorda, W. C. Sinke, and F. Spaepen, "Density of amorphous Si," *Applied Physics Letters*, vol. 64, pp. 437–439, 1994.

[67] Y. Golan, L. Margulis, and I. Rubinstein, "Vacuum-deposited gold films: I. factors affecting the film morphology," *Surface Science*, vol. 264, no. 3, pp. 312 – 326, 1992.

[68] D. Faurie, P.-O. Renault, E. L. Bourhis, and P. Goudeau, "Study of texture effect on elastic properties of Au thin films by X-ray diffraction and in situ tensile testing," *Acta Materialia*, vol. 54, pp. 4503 – 4513, 2006.

[69] C. Grovenor, H. Hentzell, and D. Smith, "The development of grain structure during growth of metallic films," *Acta Metallurgica*, vol. 32, pp. 773–781, 1984.

[70] D. Porter, K. Easterling, and M. Sherif, *Phase Transformations in Metals and Alloys.* Boca Raton: CRC Press, 3rd edition ed., 2009.

[71] D. Pashley, "The nucleation, growth, structure and epitaxy of thin surface films," *Advances in Physics*, vol. 14, no. 55, pp. 327–416, 1965.

[72] G. Long, D. Read, J. McColskey, and K. Crago, "Microstructural and mechanical characterization of electrodeposited gold films," *ASTM Special Technical Publication*, vol. 1413, 2001.

[73] M. A. Haque and M. T. A. Saif, "Deformation mechanisms in free-standing nanoscale thin films: A quantitative in situ transmission electron microscope study," *Proceedings of the National Academy of Sciences of the United States of America*, vol. 101, 2004.

[74] J. Emsley, *The Elements.* New York: Oxford University Press, 3rd ed., 1998.

[75] D. Tabor, *The Hardness of Metals.* New York: Clarendon Press, 1951.

[76] W. Zhang, S. Brongersma, O. Richard, B. Brijs, R. Palmans, L. Froyen, and K. Maex, "Influence of the electron mean free path on the resistivity of thin metal films," *Microelectronic Engineering*, vol. 76, pp. 146–152, 2004.

[77] P. Anderson and C. Li, "Hall-Petch relations for multilayered materials," *Nanostructured Materials*, vol. 5, pp. 349–362, 1995.

[78] M. H. Brodsky, R. S. Title, K. Weiser, and G. D. Pettit, "Structural, optical, and electrical properties of amorphous silicon films," *Physical Review B*, vol. 1, pp. 2632–2641, 1970.

[79] R. H. Creamer, "The measurement of the electrical resistivity of silicon," *British Journal of Applied Physics*, vol. 7, p. 149, 1956.

[80] C. Goldsmith, J. Maciel, and J. McKillop, "An update on RF MEMS switch reliability," *IEEE Microwave Magazine*, vol. 8, pp. 56–60, 2007.

[81] A. Mayadas and M. Shatzkes, "Electrical-resistivity model for polycrystalline films: the case of arbitrary reflection at external surfaces," *Physical Review B*, vol. 1, pp. 1382–1389, 1970.

[82] J. Zhang, K. Xu, and V. Ji, "Dependence of stresses on grain orientations in thin polycrystalline films on substrates: an explanation of the relationship between preferred orientations and stresses," *Applied Surface Science*, vol. 180, pp. 1 – 5, 2001.

[83] W. Zhang, S. Brongersma, O. Richard, B. Brijs, R. Palmans, L. Froyen, and K. Maex, "Microstructure and resistivity characterization of CuAu I superlattice formed in Cu/Au thin films," *Journal of Vacuum Science and Technology B: Microelectronics and Nanometer Structures*, vol. 22, pp. 2715–2718, 2004.

Appendix A

Procedure for set up and operation of the atomic force microscope

The following will outline the procedures used to obtain surface topography measurements using a diDimension®3100 AFM. This is intended to convey the methods used by the author and should not be interpreted as a replacement to the instructional materials supplied by the manufacturer.

Sample preparation and instrument set up

1. Prior to AFM measurement, the surface of the sample to be measured should be cleaned to eliminate as much debris as possible from the surface.
2. A methanol-ethanol mixture is first applied to the surface, then a drag wipe is performed using a lint free tissue.
3. The surface is then dried using high purity dry N_2 gas.
4. Both controllers must be turned on, then the computer is started.
5. While the computer boots up, ensure that the toggle switch located behind the instrument indicates STD.
6. Start the Nanoscope software, and select the correct settings by following the commands:
7. **Microscope → Profile → Tapping → Load**
8. **Microscope → Scanner → 1024g**
9. **Stage → SPM Parameters → Sample Clearance: 1000 μm → SPM Safety: 100 μm → SPM Engage Step: 0.417 μm → Load/Unload Height: 2000μm**

10. Next the cantilever holder is seated on the standard AFM station .
11. A SPM tip is then inserted into the cantilever holder, centered in the groove, and secured with the spring loaded clip .
12. Note: special care must be used when handling the SPM tips, as any sudden shock will likely break the tip.
13. With the tip installed, the cantilever holder is delicately removed from the stand and installed on the AFM head .
14. The assembly can then be secured in the dovetail, and both electrical connectors can be attached to the instrument.
15. In order for the AFM to function properly the laser must be aligned to reflect off the tip.
16. The first step is to use the x and y control knobs to place the laser on the tip.
17. Tip: raising the AFM to its highest position and placing a white piece of paper below the AFM head will enable the user to see the laser. The laser can then be scanned across the x direction until the light goes dim, allowing the user to quickly locate the tip. Fine adjustments can then be made to optimize the signal to approximately 2 V.
18. The mirror can then be adjusted to center the laser signal on the detector using the horizontal and vertical mirror adjustment knobs.
19. When properly aligned, the laser spot is centered on the AFM window, and a red dot will be centered in the vision system.
20. With the laser aligned, the sample can be placed in the vacuum chuck, and the tip can be brought above the surface by selecting Focus surface and using the trackball to move the stage.
21. While still in the Focus surface menu, the tip should be brought to within 1 cm of the surface by simultaneous holding the lower left button and rolling the trackball towards the user.
22. Next, the tip must be located in the Vision system.
23. Selecting the command focus tip allows the user to move the optical adjustment knobs and locate the tip in the cross hairs. The tip can be brought into focus using the same technique as bringing the tip closer to the surface.

24. The surface is then located by selecting the focus surface icon, and then the tip is lowered until the surface comes into focus.

25. Tip: An easy way to verify the surface is in focus is to move the stage. If the image moves as well, then the surface is in focus, but if the image does not move with the stage, then the surface is not yet in focus.

26. The final step in preparation for performing AFM scans is to tune the cantilever, which is accomplished using the auto tune function.

27. To begin, select **Cantilever Tune** → **Auto Tune**

28. Multiple auto tunes may be necessary to obtain a stable Gaussian profile.

29. Select **Center Peak** → **Zero Phase**

30. At this point, the AFM is ready to operate.

Surface topography measurement

1. Select the general area for the scan using the vision system.

2. To approach the surface, select **Engage**.

3. Once on the surface, set the scan size as appropriate, and adjust the scan speed so it is between 1 and 10 nm/s.

4. Select **Scope Mode** and observe the trace and retrace lines. They should have the same trends with very little separation.

5. Adjust the integral gain, proportional gain, and setpoint as appropriate to improve the quality of the tip tracking.

6. The scale of the image should be adjusted so the prominent features of the surface are within the limits.

7. In order to assign a filename to the image, Select **Capture** → **Capture Filename**. Then select the capture icon to begin recording the scan.

8. When the image has been captured, it is automatically saved. At this point, the tip can be withdrawn and moved to another location if desired.

9. In order to analyze the image, select the image icon.

10. Select the file desired by double clicking the filename. The image should then be corrected for curvature and slope using the flatten and plane fit features.

11. First select **Modify** → **Flatten** → **Execute** → **Quit**.

12. Then select **Modify** → **Plane Fit Auto** → **XY** → **Execute** → **Quit**.

13. To obtain surface roughness, select **Analyze** → **Roughness**.

14. In order to export an image, select **Utility** → **JPEG export**. Set background to reverse so it is white rather than the default black.

VITA

Kyle Ford

Candidate for the Degree of

Masters of Science

Thesis: AN INVESTIGATION OF THE MECHANICAL STRENGTH OF NANOCRYSTALLINE AU-SI THIN FILMS

Major Field: Mechanical Engineering

Biographical:

Personal Data: Born in Oklahoma City, OK, USA on November 14, 1987, the son of Eric and Christy Ford.

Education:
Graduated from Edmond North High School, Edmond, OK in May 2006. Received the Bachelor of Science degree in Mechanical Engineering from Oklahoma State University , Stillwater, OK in May 2010. Completed the requirements for the Master of Science in Mechanical Engineering at Oklahoma State University, Stillwater, OK in December, 2012.

Experience:
Graduate Research/Teaching Assistant, Oklahoma State University, August 2010 to December 2012.

Name: Kyle D. Ford Date of Degree: December, 2012

Institution: Oklahoma State University Location: Stillwater, Oklahoma

Title of Study: AN INVESTIGATION OF THE MECHANICAL STRENGTH OF NANOCRYSTALLINE AU-SI THIN FILMS

Pages in Study: 63 Candidate for the Degree of Master of Science

Major Field: Mechanical Engineering

A study on the effects of deposition rate and Si content on the mechanical and electrical properties of Au-Si films has been performed. Au-Si films were synthesized by electron beam evaporation on (100) Si substrates at the Center for Integrated Nanotechnologies at Los Alamos National Laboratory. The Au and Si were simultaneously codeposited to create films with a nominal thickness of 1 μm, with deposition rates from 10 Å/s to 60 Å/s and Si content up to 21 at. %. The films deposited at 10 Å/s were then investigated by transmission electron microscopy (TEM), selected area diffraction (SAD), and particle-induced X-ray emission (PIXE). All films were investigated by X-ray diffraction (XRD), atomic force microscopy (AFM), nanoindentation, and four point resistivity probe.

Nanotwinned Au grains were observed in the TEM images of the films deposited at 10 Å/s. In addition, Si nanoparticles were observed at the grain boundaries in the films containing 6 and 21 at. % Si deposited at 10 Å/s. Diffraction peaks associated with crystalline Si were not observed by SAD or XRD, which suggests the Si particles are amorphous. Grain size for the films investigated by TEM was estimated to be the average minimum length of the Au grains, where nanotwins were considered to be individual grains. Additionally, grain size was estimated using XRD for all films, and was observed to decrease with increasing Si content. Increasing deposition rate was also observed to decrease the grain size. Grain sizes determined from the TEM images were lower than those determined by XRD for the same films.

The reduced elastic modulus was found to decrease with increasing Si content for films deposited at 10 Å/s and 40 Å/s. This is consistent with the shift observed by in the diffraction intensities of the (111) and (200) Au diffraction peaks. Pure Au films were observed to have a strong (111) preferred orientation, however increasing Si content corresponded to an increase in the intensity of the (200) Au diffraction peak relative to the (111) Au diffraction peak. The reduced elastic modulus of the (200) plane in Au is less than half that of (111) plane.

The hardness of the films was observed to increase with increasing Si content. Increases in measured hardness were shown to be described by a combination of the Hall-Petch relationship and Orowan strengthening. Grain size estimates from XRD results as well as TEM images were used to predict the strength of the films using the Hall-Petch relation. Predictions based on grain size determined by XRD were shown to agree well with the measured strength of the pure Au films, while underestimating the strength of the films containing Si. Conversely, grain size estimates from the plan view TEM were shown to overestimate the film strength. For the films in which Si particles were observed, the effect of Orowan strengthening due to those particles was considered in addition to the Hall-Petch strengthening based on the grain size.

Resistivity was observed to increase linearly with Si content. Increasing deposition rate had been shown to correspond to an increase in twinning [34], which would increase film strength and decrease resistivity. However, resistivity did not decrease with increasing deposition rate, indicating that higher deposition rates did not lead to increased twinning of the Au grains.

ADVISOR'S APPROVAL: ______________________________